The individuality of shape asymmetries of the human cerebral cortex

Yu-Chi Chen[1,2*], Aurina Arnatkeviciute[1], Eugene McTavish[1,2], James C. Pang[1,2], Sidhant Chopra[1,2], Chao Suo[1,2], Alex Fornito[1,2†], Kevin M. Aquino[1,2,3,4†], for the Alzheimer's Disease Neuroimaging Initiative[‡]

[1]Turner Institute for Brain and Mental Health, School of Psychological Sciences, Monash University, Victoria, Australia 3800.

[2]Monash Biomedical Imaging, Monash University, Victoria, Australia 3800.

[3]School of Physics, University of Sydney, New South Wales, Australia 2006.

[4]Center of Excellence for Integrative Brain Function, University of Sydney, Australia 2006.

[*]Email: yu-chi.chen@monash.edu

[†]These authors contributed equally to this work.

[‡]Data used in preparation of this article were obtained from the Alzheimer's Disease Neuroimaging Initiative (ADNI) database (adni.loni.usc.edu). As such, the investigators within the ADNI contributed to the design and implementation of ADNI and/or provided data but did not participate in analysis or writing of this report. A complete listing of ADNI investigators can be found at: http://adni.loni.usc.edu/wp-content/uploads/how_to_apply/ADNI_Acknowledgement_List.pdf

Abstract

Asymmetries of the cerebral cortex are found across diverse phyla and are particularly pronounced in humans, with important implications for brain function and disease. Here, we introduce a novel approach to characterize asymmetries of the whole cortical shape across different spatial frequencies using magnetic resonance imaging data in three independent datasets. We find that cortical shape asymmetry is highly individualized and robust, akin to a cortical fingerprint, and identifies individuals more accurately than size-based descriptors, such as cortical thickness and surface area, or measures of inter-regional functional coupling of brain activity. Individual identifiability is optimal at coarse spatial scales (~37 mm wavelength), and shape asymmetries show scale-specific associations with sex and cognition, but not handedness. While unihemispheric cortical shape shows significant heritability at coarse scales (~65 mm wavelength), shape asymmetries are determined primarily by subject-specific environmental effects. Thus, coarse-scale shape asymmetries are highly personalized, sexually dimorphic, linked to individual differences in cognition, and are primarily driven by stochastic environmental influences.

Introduction

Asymmetries in brain structure and function are found throughout the animal kingdom (1-4) and can be discerned at multiple spatial scales, ranging from differences in the size and shape of the cerebral hemispheres through measures of regional morphometry and connectivity to cellular and molecular organization (2, 4, 5). At the coarsest scale, the most salient feature of anatomical asymmetry in the human brain is cerebral torque, in which the right hemisphere appears to be warped in the rostral direction relative to the left hemisphere (6-8). More fine-grained asymmetries of specific sulci/gyri (9) and brain regions (10, 11) have also been investigated. For example, the

superior temporal sulcus, which is adjacent to the Wernicke's area, shows a leftward asymmetry in length (12).

Asymmetries in brain organization are often considered at an average level across a population of individuals (7, 10, 13-15). Also called directional asymmetries (12, 16), they have been studied extensively and are thought to have important implications for both functional lateralization and abnormal brain function in a wide range of psychiatric and neurological diseases (5, 11, 15, 17, 18). However, the specific regions showing these asymmetries, their directions, and their magnitudes are often inconsistent (10, 11, 13). The correlates of these asymmetries are also unclear (4, 11, 13, 19, 20). For example, two fundamental characteristics often examined in relation to cerebral asymmetry are sex and handedness. Some studies have found that the surface area (10), shape (20-22), volume (23), and torque (8) of cortical structures in males are more asymmetric than in females, whereas other studies have found no sex differences (24, 25). Similarly, some studies have found associations between cerebral asymmetry and handedness (8, 14, 26), with others reporting no such effect (10, 11, 21, 25, 27-29).

Some of these inconsistencies may arise from the disparate methodologies and the heterogeneous nature of the brain asymmetries across the population (7, 10, 12-15). There is often considerable individual variability around population means, with many people often showing little or even reversed asymmetries relative to the group average (3, 12, 16, 30). The distinction between population-level (directional asymmetries) and individual-level asymmetries is essential, as they are thought to arise from distinct mechanisms (16, 31). Directional asymmetries are hypothesized to have a genetic basis (8, 10, 16, 30-35), whereas the degree to which a given individual departs from the population mean, referred to as fluctuating asymmetries, may reflect environmental influences, developmental plasticity, or individual-specific genetic perturbations

68 (16, 30-34, 36). Notably, fluctuating asymmetry is more pronounced in humans than other primates,
69 at both regional and global hemispheric levels (12, 30). The variability is most evident in regions
70 of heteromodal association cortex, leading some to conclude that high levels of fluctuating
71 asymmetry may have emerged in line with the evolution of human-specific cognition (12),
72 although the relationship between the fluctuating asymmetries of the human brain and individual
73 differences in cognition are still largely unknown. Traditional analysis methods, which rely on
74 standard image processing techniques such as image registration and spatial smoothing, minimize
75 individual variation and thus have limited sensitivity for studying fluctuating asymmetries (37, 38).
76 Moreover, most past works have focused on morphological properties related to the size of specific
77 brain regions, such as estimates of grey matter volume, cortical thickness, or surface area, often
78 measured at fine-grained resolutions, such as individual voxels or the vertices of cortical surface
79 mesh models (17, 19, 24, 27, 29, 39, 40). Many of the most obvious features of cerebral asymmetry
80 arise from variations in brain shape, which are not captured by size-related descriptors (21, 41).
81 Indeed, it is possible for two objects to have identical volume but have very different shapes (41,
82 42). In addition, shape variations can occur at different spatial resolution scales, from the presence
83 and configuration of specific sulci at fine scales to more global patterns such as cerebral petalia at
84 coarser scales. Conventional analyses only consider the finest resolvable scale (i.e., point-wise
85 differences) and have limited sensitivity for identifying important morphological variations that
86 occur over large swathes of cortical tissue.

87 A comprehensive, multiscale description of cortical shape, from the finest to coarsest scales,
88 can be derived through a spectral analysis of cortical geometry based on solutions to the Helmholtz
89 equation (21, 41, 43), which is fundamental in many branches of physics, engineering, chemistry,
90 and biology (51). The equation can be solved by formulating it as an eigenfunction-eigenvalue

problem of the Laplace-Beltrami operator (LBO) (see Materials and methods). Importantly, the characteristics of the eigenfunctions and eigenvalues depend on the cortical shape for which the equation is solved (43, 44), and thus, the spectral analysis provides a comprehensive description of the intrinsic geometry of a given object, akin to a "Shape-DNA" (43). The application of such Shape-DNA analysis to human magnetic resonance imaging (MRI) data has shown that shape properties of cortical and subcortical structures have superior sensitivity compared to traditional, size-based measures for identifying individual subjects (21), for classifying and predicting the progress of psychiatric and neurological diseases (38, 45), and for detecting genetic influences on brain structure (42, 46). However, a detailed characterization of fluctuating asymmetries in cerebral shape is lacking.

Here, we introduce methods for constructing an individual-specific measure of fluctuating asymmetries, called the shape asymmetry signature (SAS), that characterizes pure shape asymmetries, independent of variations in size, of the whole cortical surface across a spectrum of spatial scales. We apply this methodology to three independent longitudinal datasets to show that the SAS is a highly personalized and robust feature that can identify individuals, like a cortical asymmetry fingerprint, with greater accuracy than shape descriptors of individual hemispheres, asymmetries in traditional size-based descriptors, or patterns of inter-regional functional connectivity (so-called connectome fingerprinting (47)), thus indicating that cerebral asymmetries in shape are highly unique to individual people. Further, we use the multiscale characterization offered by spectral shape analysis to show that the optimal spatial scales for identifying individuals are expressed over coarse spatial wavelengths and not fine-grained variations in sulcal and gyral anatomy. We then show that the SAS does not covary with handedness but does differ between males and females, with some coarse scales showing a stronger rightward shape asymmetry in

114 females than males. We further demonstrate that the SAS is correlated with individual differences
115 in cognitive performance across multiple tasks. Finally, we test the hypothesis that fluctuating
116 asymmetries are largely driven by environmental influences using classical heritability modeling
117 of twin data. We show that while shape descriptors of individual hemispheres at coarse scales are
118 under significant genetic influence, shape asymmetries are primarily influenced by non-shared
119 environmental factors. Together, our results indicate that fluctuating asymmetries in cortical shape
120 are a highly unique and informative property of individual brains that are primarily sculpted by
121 non-genetic mechanisms.

122 Results

123 Cortical shape asymmetries are individually unique

124 To understand how cortical shape asymmetries vary across individuals, we examined the degree
125 to which different cortical shape descriptors can be used to identify individual brains from a large
126 sample of T1-weighted magnetic resonance images (MRIs). We analyzed healthy subjects from
127 three open-source datasets – the latest Open Access Series of Imaging Studies (OASIS-3 (48)), the
128 Human Connectome Project (HCP (49)), and the Alzheimer's Disease Neuroimaging Initiative
129 (ADNI; https://ida.loni.usc.edu/) – in which individuals had at least two anatomical MRI scans
130 acquired at different time points (separated by 18 days to several years; see Materials and
131 methods). For each dataset, we asked whether the shape descriptors for an individual estimated
132 from the first scan could accurately identify the same participant's second scan. Within each
133 dataset, the shape descriptor was calculated from the cortical surfaces at the white and grey matter
134 boundary estimated either from FreeSurfer (50) (OASIS-3 and ADNI) or FreeSurfer-HCP (HCP),
135 which is a FreeSurfer (50) pipeline with some HCP-specific enhancements (51). Shape-DNA (41,
136 43) analysis was employed to obtain multidimensional shape descriptors for each hemisphere that

137 quantify the shape of each individual's cortex, as defined by the eigenvalues spectrum of the LBO
138 (Figure 1, A and B; see Materials and methods). Each eigenvalue is associated with a
139 corresponding eigenfunction, which describes shape variations at a particular spatial wavelength,
140 ordered from coarse to fine-grained scales (Figure 1B). These eigenfunctions are orthogonal by
141 construction and thus represent a basis set for cortical shape variations much like the sinusoidal
142 basis used in Fourier decomposition of signals, with the corresponding eigenvalue being analogous
143 to the wave frequency at each spatial scale. Critically, we normalized the surface area (41) of the
144 meshes prior to Shape-DNA analysis to ensure that the resulting eigenvalue spectra were
145 independent of individual differences in brain size (see Materials and methods).

146 To investigate the uniqueness of these shape descriptors to individual brains, we performed
147 an identifiability analysis (52, 53), where identifiability was quantified as the degree to which the
148 surface eigenvalue spectrum of an individual at scan time 1 was more similar to the same person's
149 spectrum at time 2, relative to other people's time 2 spectra (Figure 1C; see also Materials and
150 methods). To determine whether identifiability is maximized at any specific scales, we repeated
151 the analysis multiple times, initially by taking only the first two eigenvalues, which describe shape
152 variations at the coarsest scale, and then incrementally adding eigenvalues representing more fine-
153 grained features to a maximum of 1000. Plotting the identifiability score as a function of the
154 number of eigenvalues allows us to identify characteristic spatial scales at which the identifiability
155 score is maximized (Figure 1D). In other words, it allows us to identify the scales at which
156 individual-specific shape features are most pronounced. We repeated this procedure using the
157 eigenvalue spectra for the left and right hemispheres alone, the combination of both (which
158 describes the shape of both hemispheres), and for the SAS, which quantifies shape asymmetries as
159 the difference between the left and right hemisphere eigenvalue spectra (see Figure 2 for details).

Finally, we utilized the spatial scales with the maximum identifiability (Figure 1D) to examine the relationships between the SAS and sex, handedness, cognition, and heritability.

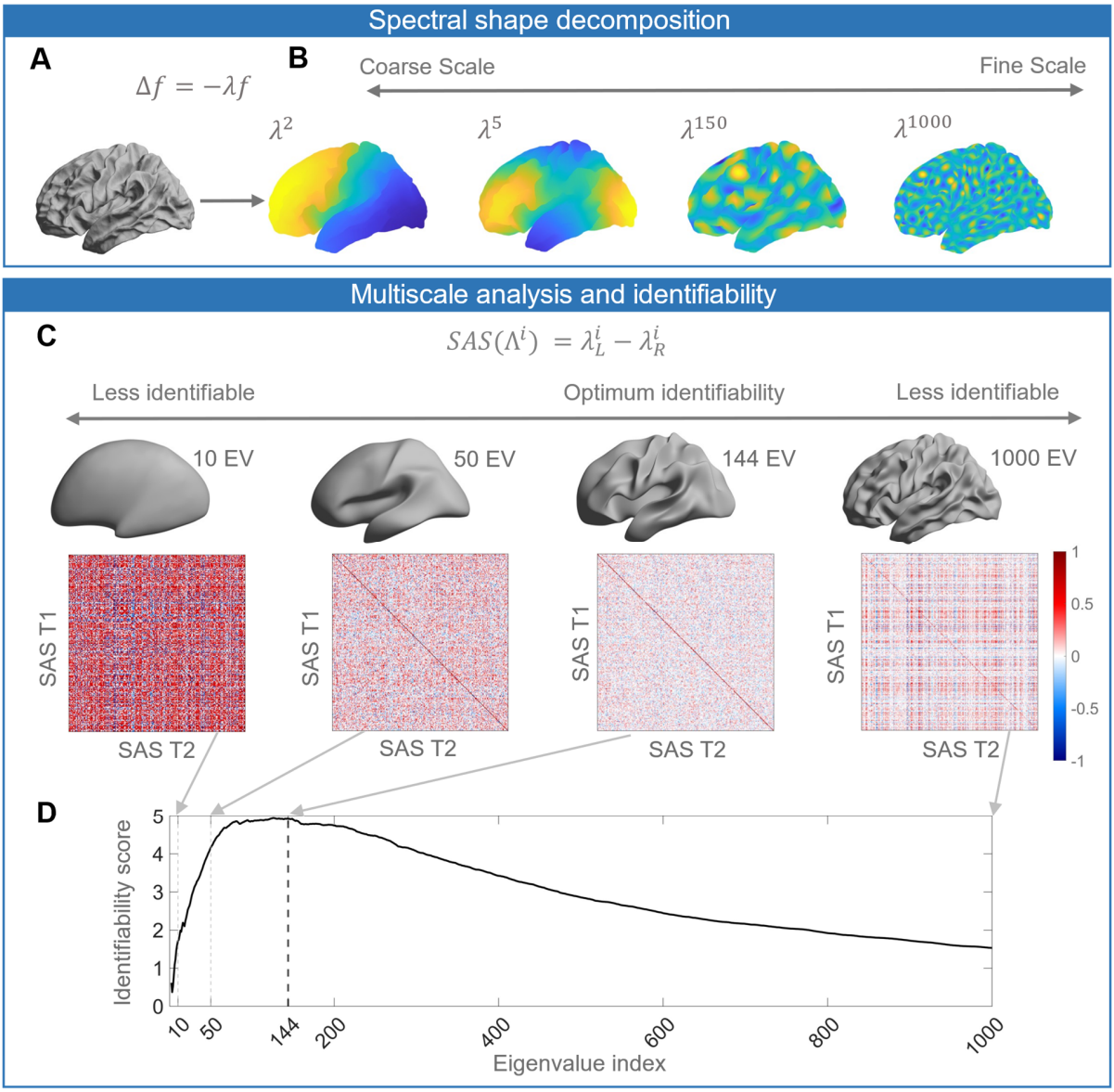

Figure 1. Schematic of our analysis workflow. (**A**) The shapes of the left and right hemispheres are independently analyzed using the Laplace-Beltrami Operator (LBO) via the Shape-DNA algorithm (41, 43). (**B**) Eigenfunctions of the LBO are obtained by solving the Helmholtz equation on the surface, given by $\Delta f = -\lambda f$, where f is corresponds to a distinct eigenfunction,

167 and λ is the corresponding eigenvalue. Each eigenvalue $\lambda^i, i = 1, 2, \ldots, 1000$, quantifies the
168 degree to which a given eigenfunction is expressed in the intrinsic geometry of the cortex.
169 Higher-order eigenvalues describe shape variations at finer spatial scales. (**C**) The Shape
170 Asymmetry Signature (SAS) is quantified as the difference in the left and right hemisphere
171 eigenvalue spectra, providing a summary measure of multiscale cortical shape asymmetries. To
172 investigate the identifiability of the SAS, we use Pearson's correlation to calculate the similarity
173 between the SAS vectors obtained for the time 1 (t1) and time 2 (t2) 2 scans from the same
174 individuals (diagonal elements of the matrices) as well as the correlation between t1 and t2 scans
175 between different subjects (off-diagonal elements). We estimate identifiability by first
176 correlating the initial two eigenvalues, then the initial three eigenvalues, and so on to a maximum
177 of 1000 eigenvalues. Here, we show examples of correlation matrices obtained when using the
178 first 10, 50, 144, and 1000 eigenvalues, and the cortical surface reconstructions show the shape
179 variations captured by corresponding spatial scales. (**D**) Repeating the identifiability analysis up
180 to a maximum of 1000 eigenvalues yields a curve with a clear peak, representing the scale at
181 which individual differences in cortical shape are maximal. For the SAS, this peak occurs when
182 the first 144 eigenvalues are used (black dashed line), which offers a fairly coarse description of
183 shape variations (see panel (C)). We then use a similar analysis approach to investigate
184 associations between scale-specific shape variations and sex, handedness, cognitive functions
185 as well as heritability. The data in this figure are from the OASIS-3 (n = 233) cohort, and the
186 cortical surfaces are from a population-based template (fsaverage in FreeSurfer).

187 Figure 2A–C shows the identifiability scores obtained for the different shape descriptors.
188 In all three datasets, across a broad range of spatial scales, identifiability was highest for the SAS,
189 followed by the combination of left and right hemisphere eigenvalues, and then each hemisphere

alone. This result indicates that individual variability in the asymmetry of cortical shape is greater than the variability of shape across the whole cortex or within each hemisphere alone. Figure 2A–C also shows identifiability scores obtained when trying to identify an individual's left hemisphere using right hemisphere shape descriptors obtained at the same time point. These scores are very low, indicating that shape variations between the two hemispheres are largely independent of each other and lack a consistent pattern amongst subjects. In other words, for any given person, the shape of one hemisphere offers little individually unique information about the shape of the other hemisphere.

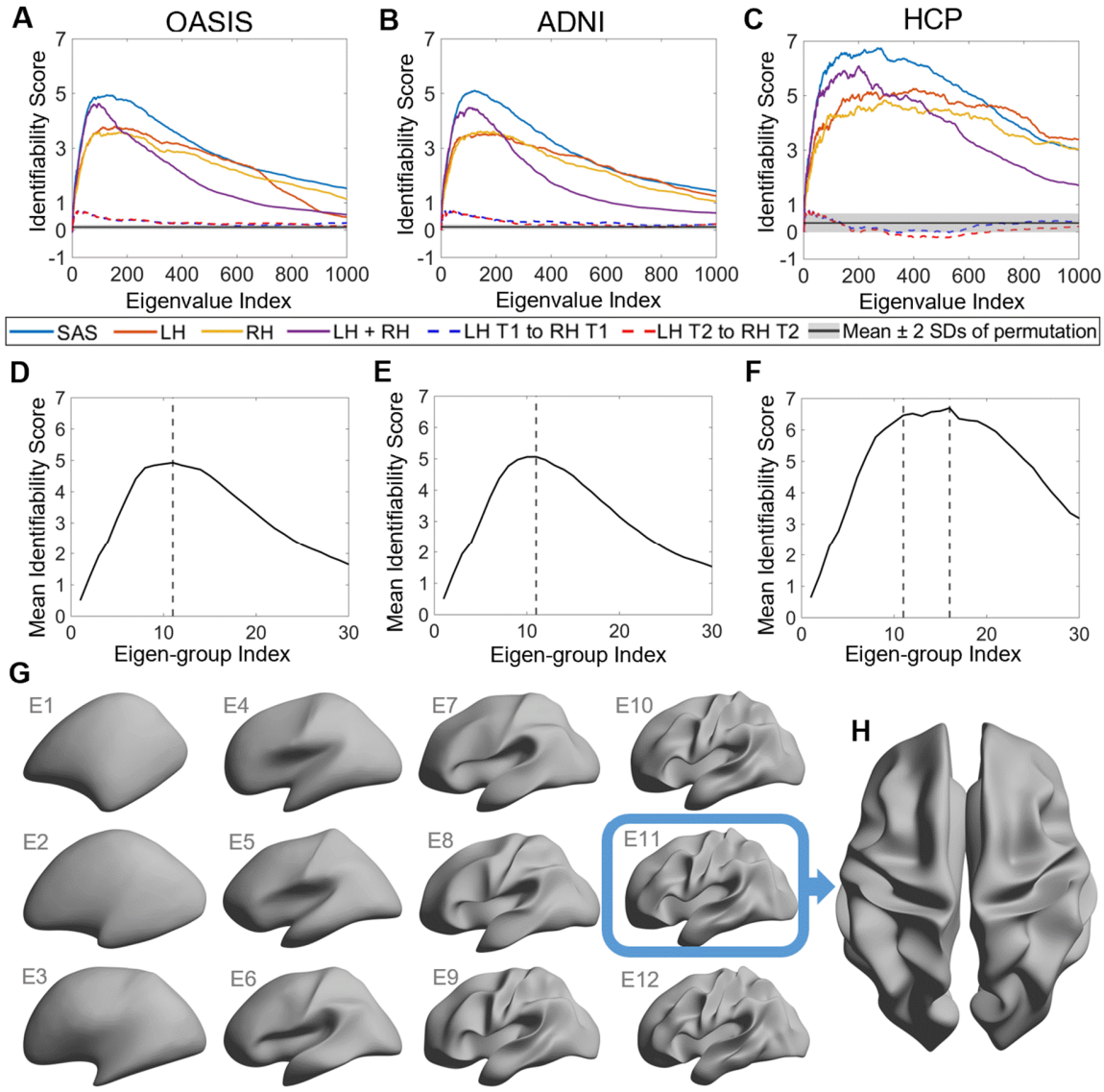

Figure 2. Identifiability of different shape descriptors at different spatial scales. **(A)** to **(C)** Identifiability scores for shape features across eigenvalue indices. The identifiability scores of the shape asymmetry signature (SAS) are generally higher than the scores for shape descriptors of individual hemispheres or scores obtained when concatenating both hemispheres across three datasets (OASIS-3: n = 233; ADNI: n = 208; HCP: n = 45). The SAS scores are also much higher than the scores obtained by randomly shuffling the order of the subjects at time 2 (shaded area represents mean ± 2 SDs). **(D)** to **(F)** The cumulative mean identifiability scores for each

206 eigenvalue group, derived from correspondence with spherical harmonics (54). The peak mean
207 identifiability occurs at the 11th eigenvalue group for the OASIS-3 (D) and ADNI data (E),
208 representing the first 144 eigenvalues. The curve of the mean identifiability score for the HCP data
209 (F) flattens after the 11th group and peaks at the 16th group. **(G)** Cortical surfaces reconstructed at
210 different spatial scales, starting with only the first eigen-group (E1) and incrementally adding more
211 groups to a maximum of the first 12 eigen-groups (E12). **(H)** Overhead view of the spatial scale
212 corresponding to the eigen-group at which identifiability is maximal in the OASIS-3 and ADNI
213 datasets (i.e., the first 11 eigen-groups, corresponding to the first 144 eigenvalues).
214 **Figure supplement 1.** Understanding the identifiability score.
215 **Figure supplement 2.** Subject identifiability scores re-calculated for data from MRI sessions with
216 the longest inter-sessional interval.

217 **Individually unique variations of cortical shape asymmetry are maximal at coarse spatial**
218 **scales**

219 We next investigated the scale-specificity of SAS identifiability. Figure 2A–C shows that SAS
220 identifiability sharply increases to a peak as we use more eigenvalues to characterize the surface
221 shape at finer scales (i.e., as we add more shape information from finer spatial scales), before
222 gradually falling again. This peak identifies a characteristic spatial scale in which individual
223 differences in shape asymmetries are maximally unique (see also Figure 2—figure supplement 1).
224 Peak SAS identifiability was observed using the first 126 and 122 eigenvalues for the
225 OASIS-3 (Figure 2A) and ADNI (Figure 2B) data, respectively. At these scales, the subject
226 identifiability scores were 4.93 ($P = 0$) for OASIS-3 and 5.03 ($P = 0$) for ADNI. For the HCP data,
227 peak SAS identifiability was observed when using the first 268 eigenvalues (identifiability score

228 = 6.74; P = 0; Figure 2C), but the identification curve flattened after the first 137 eigenvalues
229 (identifiability score = 6.56), which is closely aligned with the OASIS-3 and ADNI datasets.

230 In the case of a perfect sphere, the shape spectral analysis yields subsets of degenerate
231 eigenvalues with equal magnitude (54), within which the corresponding eigenfunctions represent
232 orthogonal rotations of the same spatial pattern at a given scale. For example, eigenfunctions 2–4
233 of a sphere represent coarse-scale gradients in the anterior-posterior, inferior-superior, and left-
234 right axes. As the cortex is topologically equivalent to a sphere, the spherical eigen-groups offer a
235 natural way to identify characteristic spatial scales, to more succinctly summarize cortical shape
236 variations (54), and to smooth out eigenvalue-specific fluctuations at a given scale (see Materials
237 and methods). We averaged the identifiability scores for each harmonic group and plotted these as
238 a function of the group index in Figure 2D–F. The group mean identifiability score peaks at the
239 11th eigenvalue group for the OASIS-3 (mean identification score = 4.93) and ADNI (mean
240 identifiability score = 5.06) datasets, which is comprised of the first 144 eigenvalues. Identifiability
241 also reaches a near-plateau at the 11th group for the HCP data (mean identifiability score = 6.47),
242 with an additional marginal increase observed at the 16th group (mean identifiability score = 6.69).
243 Thus, the first 144 eigenvalues represent a stable and robust characteristic scale at which individual
244 uniqueness in cortical shape asymmetry is strongest. The 11th group corresponds to a wavelength
245 of approximately 37 mm in the case of the population-based template (fsaverage in FreeSurfer;
246 Appendix 1—Table 1 shows the corresponding wavelengths of the first 14 eigen–groups; Figure
247 2G shows the spatial scales corresponding to the cumulative eigen-groups). A reconstruction of
248 the cortical surface using the first 144 eigenfunctions is shown in Figure 2H. The reconstruction
249 captures shape variations at a coarse scale, representing major primary and some secondary sulci
250 but with minimal additional details. This same characteristic scale was obtained after repeating the

identifiability analysis over the longest inter-scan intervals in the ADNI and OASIS-3 datasets (Figure 2—figure supplement 2), indicating that our results are robust over time windows ranging from 18 days to more than six years.

Shape asymmetries are more identifiable than classical morphological and functional measures

We next compared the identifiability of the SAS to scores obtained using asymmetries in classical morphological descriptors such as regional surface area, cortical thickness and grey matter volume, and measures of inter-regional functional connectivity (Figure 3), which have previously been shown to yield high identifiability (47, 52). Identifiability scores obtained with the SAS were much higher than those obtained by regional asymmetries in size-related morphological measures with the HCP-MMP1 atlas (55) (Figure 3, A and B). We also found that SAS identifiability was higher when using our surface area normalization procedure compared to the SAS computed without this procedure (Figure 3—figure supplement 1; see Materials and methods). Since the normalization isolates the pure effects of shape independent of brain size, the results converge to indicate that individual variability in brain anatomy is higher when considering asymmetries in cortical shape compared to more traditional size-based morphological descriptors.

Figure 3C–F compares the identifiability scores obtained from SAS to those obtained using inter-regional functional connectivity (see Materials and methods), within the HCP test-retest data. Functional connectivity was quantified for the entire cortex using four different regional parcellations defined at different spatial scales (Schafer 100, Schaefer 300, Schaefer 900 (56), and HCP-MMP1 (55) atlas). The SAS outperformed all functional identifiability scores, indicating that cortical shape shows greater specificity to an individual than patterns of functional connectivity.

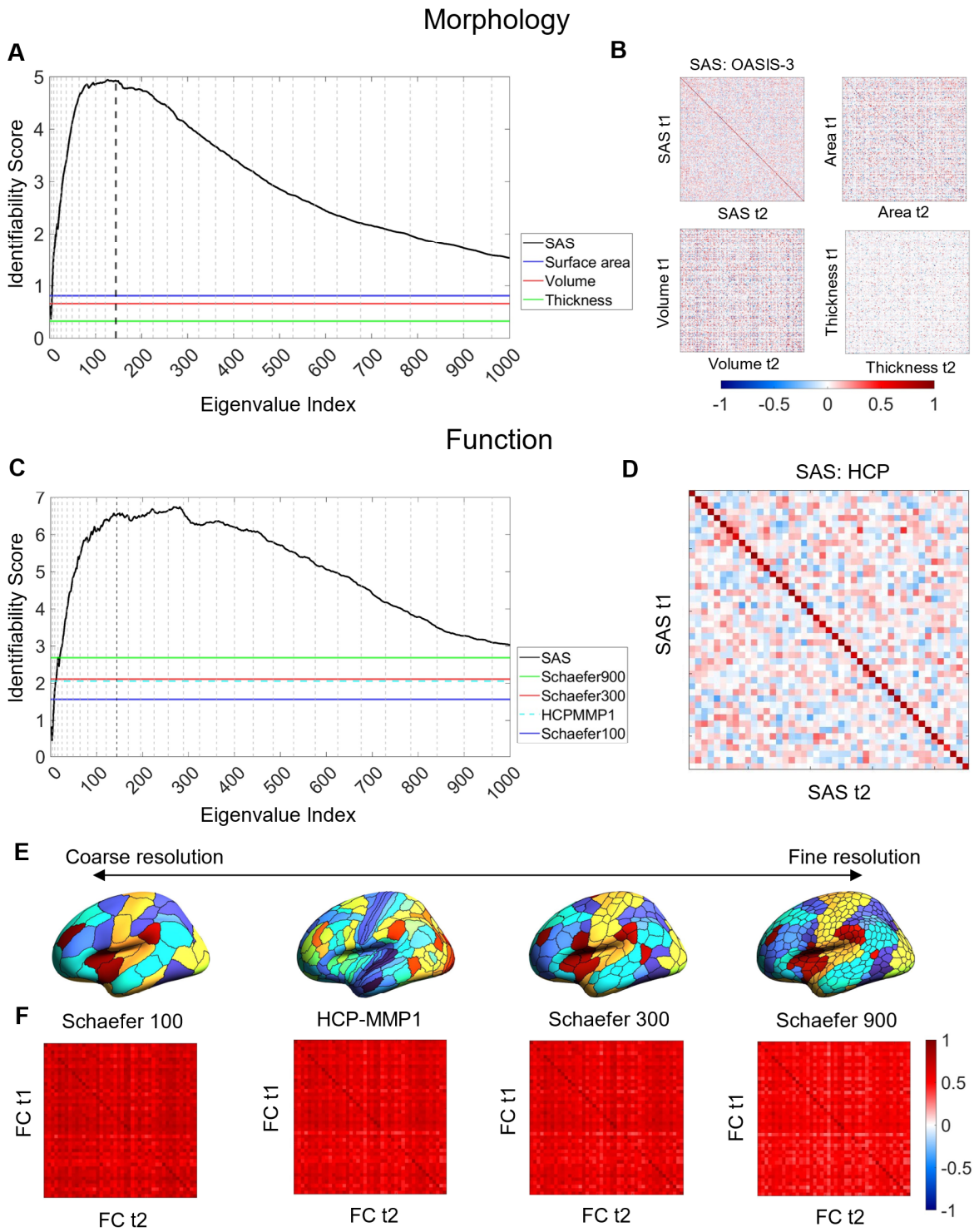

Figure 3. Cortical shape asymmetries are more identifiable than size-related descriptors or functional connectivity. **(A)** Identifiability scores for the SAS are higher than those obtained for

asymmetries based on cortical surface area (identifiability score = 0.81), volume (identifiability score = 0.66), and thickness (identifiability score = 0.33) for the OASIS-3 dataset (n = 232; see Materials and methods). **(B)** Matrices of the Pearson correlation coefficients for shape asymmetry signatures and size-based morphological asymmetries from MRI scans taken at different time points (t1 and t2) of the OASIS-3 subjects. **(C)** SAS identifiability is higher than the identifiability based on functional connectivity, assessed with parcellations at different resolution scales in the HCP test-retest dataset (n = 44). **(D)** Matrix of the Pearson correlation coefficients for shape asymmetry signatures of the HCP subjects. **(E)** Four resolution scales of parcellations used in the functional connectivity analysis (shown on an inflated fsaverage surface in FreeSurfer). **(F)** Matrices of the Pearson correlation coefficients for functional connectivity using the Schaefer 100 (identifiability score = 1.57), HCP-MMP1 (identifiability score = 2.06), Schaefer 300 (identifiability score = 2.11), and Schaefer 900 (identifiability score = 2.69) parcellations.

Figure supplement 1. Comparing identifiability scores between the shape asymmetry signature (SAS) with either native eigenvalues or volume-normalized eigenvalues.

Cortical shape asymmetries are related to sex but not handedness

Sex and handedness are two characteristics that have frequently been examined with brain asymmetry (2, 7, 10, 11, 21, 23, 25, 27, 57). We used a general linear model (GLM) with permutation testing and accounting for familial structure (58, 59) of the HCP data to evaluate the association between these two characteristics and the SAS defined at each eigenvalue ranging between the 2nd and 144th. After FDR correction, males and females showed significant differences in asymmetry scores for the 2nd (P_{FDR} = 0.037), 6th (P_{FDR} = 0.037), 8th (P_{FDR} = 0.039), 52nd (P_{FDR} = 0.030), and 84th (P_{FDR} = 0.037) eigenvalues (Figure 4A), where female brains showed more rightward asymmetric than males in these eigenvalues. These five eigenvalues come from four

different eigen-groups, and the corresponding spatial scales of these eigenvalues are shown in Figure 4B. These eigenvalues relate to shape variations over coarse scales. For instance, for the 2nd eigenvalue ($L = 1$; see Materials and methods for the definition of L), the wavelength is of order 300 mm, which is about half the circumference of the brain; for the most-fine grained eigenvalue, the 84th eigenvalue ($L = 9$), the wavelength is about 44 mm. We note however that the sex differences are small, with considerable overlap between male and female distributions (Figure 4A). No such effects of handedness on the SAS surpassed the FDR-corrected threshold. We also found that the overall asymmetry level (i.e., the sum of the SAS) was not correlated with either handedness or sex.

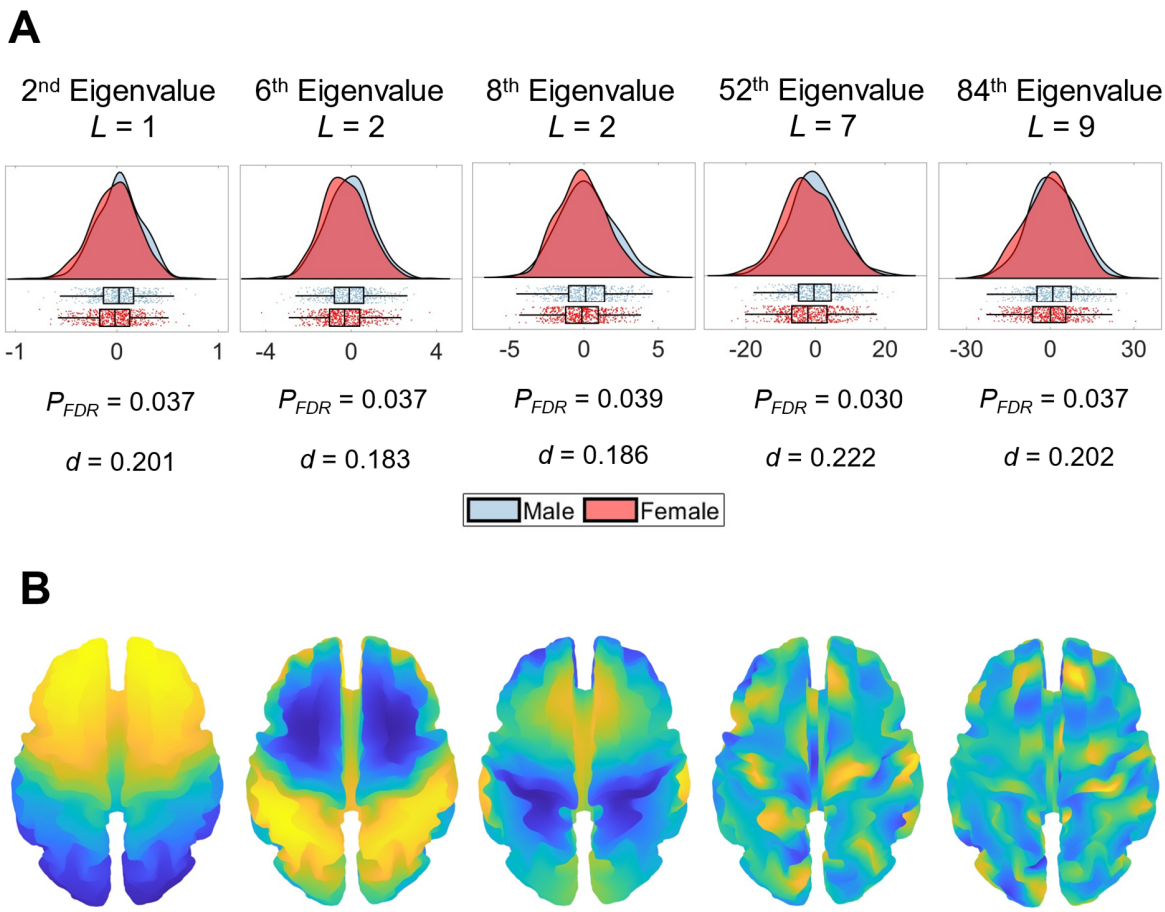

Figure 4. Sex differences in eigenvalue asymmetries. (**A**) Smoothed distributions and boxplots with mean and interquartile range (60) of the eigenvalues among males (n = 504) and females (n = 602). Under these five spatial scales, female brains show a greater rightward asymmetry than males. The *p*-values are FDR-corrected values of the correlation between sex and SAS, obtained via a GLM. The *d* values are effect sizes (Cohen's *d*). *L* denotes eigen-group. (**B**) The corresponding eigenfunction of each eigenvalue in panel (A) shown on a population-based template.

Individual differences in cortical shape asymmetry correlate with cognitive functions

We used canonical correlation analysis (CCA) (61) to examine associations between the SAS and 13 cognitive measures from the HCP dataset (n = 1094; see Materials and methods) selected to represent a wide range of cognitive functions ((62); see Materials and methods for details). To reduce the dimensionality of the SAS measures and ensure equivalent representation of asymmetries at each spatial scale, we took the mean SAS value for each of the 1st to 11th eigen-groups, spanning the 2nd to 144th eigenvalues. To minimize collinearity of the cognitive variables, we applied principal component analysis (PCA) to the 13 cognitive measures and retained the first four principal components (PCs), which explained 80% of the variance. The analysis revealed a single statistically significant canonical mode (CCA $r = 0.187$; $P_{FWER} = 0.032$; Figure 5A). Figure 5B shows that the mode has significant positive loadings from mean SAS scores in eigen-groups 2, 4, 5, and 11, and significant negative loadings from eigen-groups 3, 6, 7, 10. Figure 5C indicates that 12 of the 13 cognitive measures showed significant positive correlations with the canonical variate, indicating that it captures covariance with general cognitive ability. Thus, our findings identify strong scale-specificity of associations between cortical shape asymmetry and cognition, with a greater leftward asymmetry in scales captured by eigen-groups 2 (~170 mm wavelength), 4

(~95 mm wavelength), 5 (~75 mm wavelength), and 11 (~37 mm wavelength) being associated with better performance across most cognitive measures, and a greater leftward asymmetry in scales captured by eigen-groups 3 (~120 mm wavelength), 6 (~65 mm wavelength), 7 (~55 mm wavelength), and 10 (~40 mm wavelength) being associated with poorer cognitive performance.

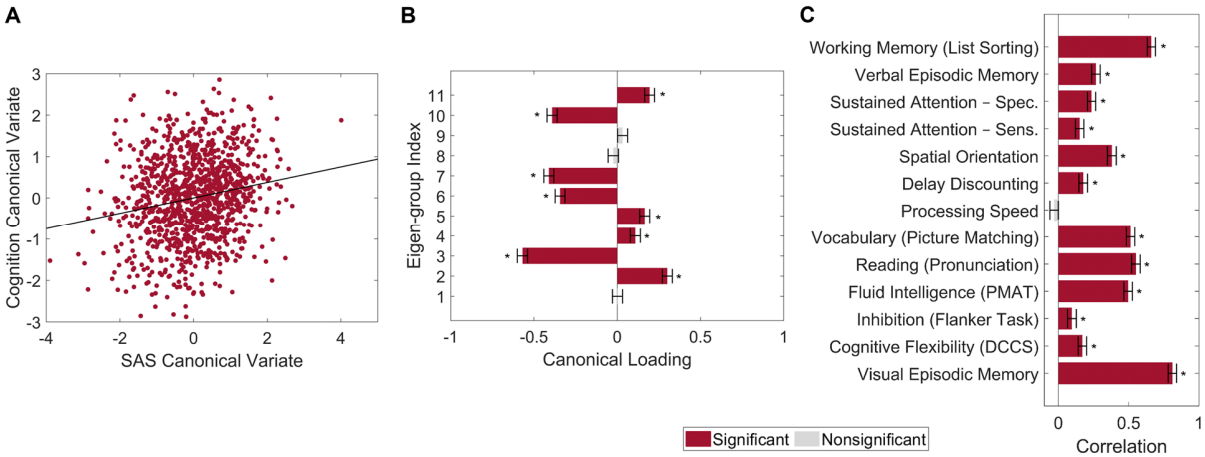

Figure 5. Individual differences in cortical shape asymmetry correlate with general cognitive ability. **(A)** Scatterplot of the association between the cognitive and SAS canonical variates with the corresponding least-squares regression line in black. **(B)** Canonical variate loadings of each eigen-group. **(C)** Correlations between the original cognitive measures and the cognitive canonical variate. Error bars show $\pm$ 2 bootstrapped standard errors (SE). Asterisks denote bootstrapped $P_{FDR} < 0.05$.

Cortical shape asymmetries are primarily driven by unique environmental influences

To characterize genetic and environmental effects on cortical shape and its asymmetry, we calculated the heritability of each eigenvalue within the left and right hemispheres, as well as for the SAS. We used data from 138 monozygotic (MZ) twin pairs, 79 dizygotic (DZ) twin pairs, and 160 of their non-twin siblings drawn from the HCP dataset (49) (see Materials and methods for details). Uni-hemispheric shape descriptors demonstrated strong heritability at very coarse spatial

scales and moderate heritability at slightly finer scales. For instance, the heritability of the 1st eigen-group (2nd to 4th eigenvalues) of both hemispheres ranged between $0.52 < h^2 < 0.69$ (all $P_{FDR} < 0.05$; Figure 6, A and B). These eigenvalues are related to shape variations on the coarsest scale that does not include any sulcal or gyral features (the corresponding wavelength is approximately 170 mm). Beyond the 2nd eigen-group, heritability estimates dropped to below 0.5 ($P_{FDR} < 0.05$ for most eigenvalues), and beyond the 4th eigen-group they dropped below 0.3. Most eigenvalues with statistically significant heritability estimates were confined to the first six eigen-groups, which correspond to wavelengths greater than or equal to approximately 65 mm (Figure 6, A and B insets). These results indicate that genetic influences on the shape of each cortical hemisphere are expressed over very coarse scales at which only primary cortical folds such as the Sylvian and central sulci are apparent. Estimates of common environmental influence on both hemispheres were uniformly low across the 2nd to 144th eigenvalues (range 0–0.20).

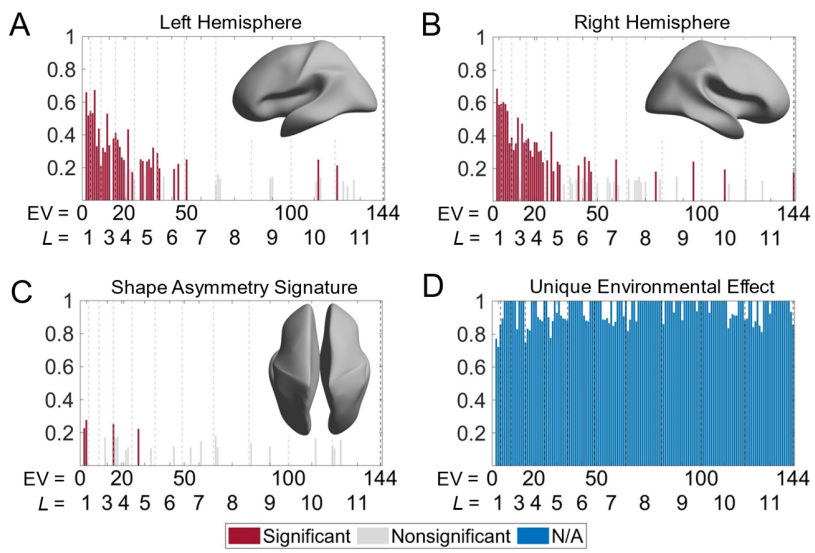

Figure 6. Heritability of cortical shape. **(A)** and **(B)** Heritability of the eigenvalues of the left (A) and right (B) hemispheres. The insets show the corresponding spatial scales by reconstructing the

surfaces using the first six eigen-groups. **(C)** Heritability of the SAS. The inset shows the corresponding spatial scale with some level of genetic influence, obtained by reconstructing the surface using the first five eigen-groups. **(D)** Unique environmental influences to the SAS at each eigenvalue. Statistical significance is evaluated after FDR-correction. Note that significance is not estimated for unique environmental effects as this represents the reference model against which other genetically informed models are compared. We use 79 same-sex DZ twin pairs, 138 MZ twin pairs, and 160 of their non-twin siblings.

Figure supplement 1. Heritability of cortical shape with volume normalization but without normalizing the surface area.

Figure supplement 2. Heritability estimates of regional volumes of individual hemispheres across four parcellation resolutions.

In contrast to unihemispheric shape variations, all the heritability estimates of the SAS were low (<0.28; Figure 6C), with only four eigenvalues (2, 3, 16, and 28) showing statistically significant heritability after FDR correction (P_{FDR} = 0.004 to 0.022) and no heritability estimates exceeding 0.30. Thus, at any given scale, genes account for less than one-third of the phenotypic variance in the SAS. These four eigenvalues are confined to the first five eigen-groups, with corresponding wavelengths greater than or equal to approximately 75 mm (Figure 6C inset). Estimates of common environmental influences were uniformly low (range 0–0.14), whereas unique (subject-specific) environmental influences on the SAS were consistently high across the full range of eigenvalues considered, ranging between 0.72 to1.00 (Figure 6D).

Notably, heritability estimates for non-surface area normalized eigenvalues of individual hemispheres, which capture variations in both shape and size, were uniformly high across all scales, and the scale-specific effects were eliminated (Figure 6—figure supplement 1), indicating

387 that variations in cortical size are under greater genetic influence than cortical shape. The results
388 underscore the importance of controlling for size-related variations in shape analyses.

389 Discussion

390 Asymmetries in brain anatomy are widely viewed as a critical characteristic for understanding
391 brain function. Here, we employed a multiscale approach to examine fluctuating shape
392 asymmetries of the human cerebral cortex. We found that fluctuating asymmetries were highly
393 personalized and robust, with shape asymmetries at coarse spatial scales being the most
394 discriminative among individuals, showing differences between males and females, and
395 correlating with individual differences in cognition. Heritability estimates of shape descriptors in
396 individual hemispheres were high at very coarse scales but declined to moderate values at finer
397 scales. By contrast, the heritability of fluctuating asymmetries in shape was low at all scales, with
398 such asymmetries being predominantly influenced by individual-specific environmental factors.

399 Identifiability of cortical shape asymmetry is maximal at coarse scales

400 Cortical asymmetries have traditionally been investigated at fine-scale, voxel or vertex-level
401 resolutions (17, 19, 24, 27, 29, 39, 40). These approaches may ignore meaningful effects at coarser
402 spatial scales. Our SAS quantifies these underlying variations across the whole brain and along a
403 spectrum of spatial scales. Our approach is akin to studying seismic waves of earthquakes with
404 different wave frequencies at the global tectonic scale, instead of focusing on a particular city. The
405 ability to assess shape along a spectrum of spatial scales is important, since brain asymmetry is a
406 multidimensional and multivariate phenotype (3, 13, 39).

407 Few studies have assessed shape at coarse scales. Neubauer et al. (30) found that
408 fluctuating asymmetry in endocranial shape is reliable across two time points. The endocranial

409 shape is the imprint of the cortical surface shape but contains only very coarse shape information
410 (30). Moreover, levels of brain torque (both horizontal and vertical) are robust across time (57).
411 Wachinger et al. (21) used shape descriptors at coarse scales derived from the eigenvalues of the
412 LBO for all brain structures to achieve accurate subject identification.

413 It is perhaps surprising that individual differences in cortical shape are most strongly
414 expressed at coarse scales, given the known variability of fine-grained anatomical features such as
415 the presence and trajectories of secondary and tertiary sulci. It is possible that these fine-grained
416 features are not captured reliably, meaning that they contribute noise to identifiability analyses.
417 Traditional analysis methods use smoothing to address the issue of image noise (40), but
418 smoothing can also suppress the actual variations at fine scales. Our multiscale approach affords a
419 more comprehensive characterization of shape variations and their uniqueness. An important
420 avenue of future work will involve investigating the functional consequences of these pronounced
421 individual differences.

422 **Cortical shape, rather than shape asymmetry, is heritable**

423 Genetic effects on cortical thickness and surface area are generally bilateral (10, 63-65), resulting
424 in few lateralized effects (10, 66). Accordingly, it has been postulated that fluctuating asymmetries
425 may be largely determined by environmental factors (16, 31-34). In line with this hypothesis, we
426 found that fluctuating asymmetries in cortical shape were associated with low heritability and were
427 driven mainly by unique environmental effects. These environmental effects are captured by the
428 *E* parameter of the *ACTE* heritability model that we used in our analysis; this parameter also
429 includes the contributions of measurement error. However, our effects cannot be explained by the
430 SAS being a noisier descriptor of morphology as it showed the highest identifiability (Figure 2A–
431 C). That is, a noisy measure will not be able to discriminate between individuals. Thus, taking the

findings of our identifiability and heritability analyses together, we can conclude that individual differences in SAS scores are primarily driven by unique environmental influences rather than measurement error. Previous studies have found some evidence of environmental influences on brain asymmetry (2, 4, 5, 67). Early in the intrauterine environment, fetal posture and light may influence brain asymmetry (2, 4, 5); during postnatal maturation, language learning has been linked to specific asymmetry features. For example, bilinguals have stronger rightward asymmetry of cortical thickness of the anterior cingulate than monolinguals (67). However, the mechanisms of how environmental effects shape brain asymmetry are largely unknown, and epigenetics may also play a role (2, 4).

In contrast to shape asymmetries, the shape of individual hemispheres showed greater heritability at coarse scales, consistent with results from previous studies on other morphological measurements (10, 35, 39). The scales at which genetic effects on unihemispheric shape were observed captured variations in primary sulci, consistent with evidence that the primary folds, which develop early in life, are less variable across individuals and under greater genetic control than other folds (i.e., secondary and tertiary folds) (39, 68, 69). Previous studies have found that genetic influences on the cerebral thickness, geodesic depth, and surface curvature generally occur along the posterior–anterior and inferior–superior axes (39, 70). These two axes correspond to the second and third eigenvalues of the LBO, which also showed strong heritability in the shapes of both hemispheres in our results. In addition to these two axes, we found strong heritability at very coarse scales in other directions that have not been described in previous studies. Our approach thus identifies dominant spatial scales and gradients of heritability in shape.

453 **Shape asymmetries, sex, and handedness**

454 Using our multiscale approach, we did not find a relationship between shape asymmetry and
455 handedness, consistent with numerous studies showing that handedness is unrelated to anatomical
456 brain asymmetry in cortical thickness, volume, surface area, shape, and voxel-based morphometric
457 (VBM) analysis (10, 11, 20, 21, 25, 27, 29).

458 Numerous studies, focusing primarily on size-related descriptions such as grey matter
459 volume and cortical thickness, have found that female brains are more symmetric than male brains
460 (8, 10, 20-23). Our analysis reveals that, although the overall level of shape asymmetry did not
461 differ between male and female brains, female brains displayed a greater rightward shape
462 asymmetry than male brains at certain coarse spatial scales, such as along the anterior-posterior
463 axis. The mechanisms giving rise to these scale-specific sex differences require further
464 investigation.

465 **Shape asymmetries are correlated with general cognitive performance**

466 We found that the individual differences in cortical shape asymmetry are correlated with cognitive
467 performance in a scale-specific way. Specifically, we found that a greater leftward asymmetry
468 across a wide range of spatial scales, corresponding to wavelengths of approximately 37, 75, 95,
469 and 170 mm, and greater rightward asymmetry at wavelengths of approximately 40, 55, 65, and
470 120 mm, are associated with better performance across nearly all cognitive measures considered.
471 Previous studies have found that fluctuating asymmetries in cortical thickness and surface area are
472 negatively correlated with cognition (36, 71), but these studies only measured the level of
473 asymmetry and did not consider the direction (i.e., leftward or rightward) of the asymmetry. The

474 scale-specificity of the associations that we find underscore the importance of viewing brain
475 asymmetry as a multiscale rather than a unidimensional trait.

476 The magnitudes of the associations are modest, but they are consistent with effect sizes
477 reported in past works (36, 71). These modest correlations with cognition may reflect a robustness
478 of cognitive abilities to stochastic perturbations of brain morphology, given that our heritability
479 analysis revealed a dominant effect of unique environmental factors in driving individual
480 differences in cortical shape asymmetries.

481 Conclusion

482 We developed a multiscale approach and found that fluctuating asymmetries in cortical shape are
483 robust and personalized neuroanatomical phenotypes, especially at coarse spatial scales. Some of
484 these coarse scales are more strongly rightward asymmetric in females compared to males. The
485 fluctuating shape asymmetries also show scale-dependent associations with cognition. Finally,
486 fluctuating asymmetries in cortical shape are driven mainly by subject-specific environmental
487 influences rather than by genetics, unlike the shape of individual hemispheres that shows strong
488 heritability at coarse scales.

489 Materials and methods

490 Neuroimaging data

491 We used healthy subject data from three open-source neuroimaging datasets: the latest Open
492 Access Series of Imaging Studies (OASIS-3 (48)), the Human Connectome Project (HCP (49)),
493 and the Alzheimer's Disease Neuroimaging Initiative (ADNI; https://ida.loni.usc.edu/) to develop
494 and test our new asymmetry shape measure – the SAS (see below for details). To test for

relationships of sex, handedness, and heritability, we restricted our analysis to the HCP dataset, which provides twin and non-twin sibling information and handedness measurement as a continuous variable, as the sample sizes of the left-handers in the other two datasets are too small (n = 15 in the ADNI data; n = 18 in the OASIS-3 data).

OASIS-3

We used 239 healthy participants with at least two longitudinal MRI sessions using 3T scanners from the latest release of the Open Access Series of Imaging Studies (OASIS-3) (48). We excluded six subjects whose SAS was an outlier in at least one of those sessions due to poor image quality and major errors in image segmentation. These subjects had more than two eigenvalues of the first 200 eigenvalues that departed from the population mean values by more than four standard deviations. The remaining 233 subjects (99 males; 134 females) were aged from 42 to 86 (mean = 66.03; standard deviation = 8.81) when they entered the study. We also repeated the analyses using all the subjects including the outliers, and the resulting number of eigenvalues with peak identifiability was identical to the initial analysis that excluded the outliers. For comparing the identifiability of the SAS and the asymmetry from traditional measurements (volume, cortical thickness, and surface area), we further excluded one subject because some of this subject's files were corrupted and could not be segmented. For subjects with more than two MRI sessions (n = 115), our main analysis used the initial session as the time 1 (t1) session and the session closest in time to the initial session as the time 2 (t2) session. The mean interval between these two sessions was 2.95 years (standard deviation = 1.71 years). To ensure the robustness of our methods, we used sessions with the longest intersession interval (mean interval of 6.21 years; standard deviation of 1.90 years) to re-analyze the subject identifiability. These healthy participants had no history of neurological or psychiatric diseases. We also excluded subjects with a Mini-Mental State

518 Examination (MMSE) score equal to or lower than 26, as this indicates that a subject is at risk of
519 being diagnosed with dementia (72). OASIS-3 (48) provides surface meshes based on the T1-
520 weighted MRI images created by FreeSurfer version 5.3 with the cross-sectional pipeline (i.e., to
521 treat the T1 and T2 sessions independently (50)), including the FreeSurfer patch (10Dec2012) and
522 the Human Connectome Project (HCP) patch
523 (http://surfer.nmr.mgh.harvard.edu/pub/dist/freesurfer/5.3.0-HCP) (48). A trained lab member of
524 the OASIS project reviewed the image segmentation, and for the images that failed the quality
525 control, TkMedit (http://freesurfer.net/fswiki/TkMedit), a FreeSurfer toolbox, was used to revise
526 the images and re-run the FreeSurfer pipeline (48). After the re-segmentation, the images were
527 excluded if they still failed a quality control process (48). The details of the OASIS-3 dataset can
528 be found in LaMontagne et al. (48) and the OASIS website (https://www.oasis-brains.org/). We
529 used the actual output files provided by the OASIS-3 without any further corrections.

530 *HCP*

531 We used participants from the Human Connectome Project (HCP) (49) s1200 release
532 (www.humanconnectome.org/), which includes 1113 subjects with T1-weighted MRI. All subjects
533 of the s1200 release were healthy young adults (aged 22–35, mean = 28.80, standard deviation =
534 3.70). The structural images (T1-weighted and T2-weighted scans) of the HCP have a high
535 isotropic resolution (0.7 mm; see (49) for details), and all images underwent the HCP-specific
536 minimal preprocessing pipeline (51). We used native surface meshes created by the FreeSurfer
537 (version 5.3)-HCP pipeline (50, 51, 73, 74) from T1-weighted MRI images using 3T scanners. For
538 subject identification, we employed the test-retest subsample, which consists of 45 healthy subjects
539 (13 males, 32 females) aged from 22 to 35 (mean = 30.29; standard deviation = 3.34), including
540 17 pairs of monozygotic twins. The intervals between the test session (the t1 session in our

541 analysis) and the retest session (t2) were between about one to 11 months (mean interval of 4.7
542 months). To compare the identifiability of the SAS and the resting-state functional connectivity,
543 we further excluded one subject without REST1 data in one session.

544 For analyzing the relationships between SAS and sex as well as handedness, we excluded
545 three subjects with unclear zygosity and four subjects with outlying SAS values (using the same
546 criteria as used in the OASIS-3) from the s1200 release subjects, and general linear modeling
547 (GLM) of sex and handedness effects were applied to cross-sectional data of these remaining 1106
548 subjects (504 males; 602 females). We further excluded 12 subjects who did not have all 13
549 cognitive measures analyzed in our CCA (detailed below). Among the s1200 release subjects were
550 79 same-sex dizygotic twin (DZ) pairs and 138 monozygotic twin (MZ) pairs; 160 of these twin
551 pairs have non-twin sibling imaging data. For twin pairs with more than one non-twin sibling, we
552 selected one sibling at random (75). We used the resulting twin and non-twin siblings data for the
553 heritability analysis.

554 *ADNI*

555 The Alzheimer's Disease Neuroimaging Initiative (ADNI) database (adni.loni.usc.edu) was
556 launched in 2003 as a public-private partnership, led by Principal Investigator Michael W. Weiner,
557 MD. The primary goal of ADNI has been to test whether serial magnetic resonance imaging (MRI),
558 positron emission tomography (PET), other biological markers, and clinical and
559 neuropsychological assessment can be combined to measure the progression of mild cognitive
560 impairment (MCI) and early Alzheimer's disease (AD).

561 Participants in the ADNI sample completed multiple MRI sessions, but the number of
562 sessions was not consistent across subjects. We used 208 healthy control subjects from the ADNI

1 who had both the baseline MRI session (the t1 session) and a follow-up MRI session six months later (the t2 session). These subjects comprised 109 males and 99 females aged 60 to 90 (mean = 76.21; standard deviation = 5.10) upon study entry. Of these 208 subjects, 135 subjects also had an MRI session three years later from the initial session. To evaluate the stability of our methods, we re-analyzed these 135 subjects using data from the 3-year follow-up as the t2 session. The preprocessing procedure included gradwarping, B1 correction, and/or N3 scaling. We used the ADNI provided surface meshes generated by the cross-sectional FreeSurfer (version 4.3) from T1-weighted MRI image. Detailed descriptions of image acquisition, quality control, and preprocessing are described at http://adni.loni.usc.edu/methods/mri-tool/mri-analysis/ and (76).

Spectral shape analysis

We utilized the eigenvalues of the LBO applied to cortical surface mesh models generated with FreeSurfer (50). The eigendecomposition of each individual's cortical surface was estimated using the Shape-DNA software (21, 41, 43), which provides algorithms that extract and optimize the eigenvalues and eigenfunctions from the LBO based on the intrinsic shape of an object (41, 43). The Shape-DNA software (41, 43) uses the cubic finite element method to solve the Helmholtz equation (Eqs. 1), also known as the Laplacian eigenvalue problem:

$$\Delta f = -\lambda f \qquad (1)$$

where Δ is the LBO; f is the eigenfunction with corresponding eigenvalue λ. The eigenvalues of the Helmholtz equation are a sequence ranging from zero to infinity, i.e., $0 \leq \lambda^1 \leq \lambda^2 \leq \ldots < \infty$, and changes in shape result in changes in the eigenvalue spectrum (43).

Spectral shape analysis via LBO is a departure from traditional morphological analyses that focus on either specific locations (i.e., regions defined by a cortical atlas) or global differences

585 (such as total hemispheric volume). Spectral shape analysis focuses instead on differences in the
586 spatial scales of variation. The decomposed spatial scales can be linearly combined to reconstruct
587 the surface via the eigenfunctions and their corresponding coefficients (the contribution of each
588 set of eigenfunctions to the original surface; see Figure 2G for examples of reconstructed surfaces).
589 Importantly, Shape-DNA achieves better results for retrieving object shapes than numerous
590 cutting-edge shape-retrieval methods (77). Shape-DNA compresses the cortical-surface geometry
591 from around 5 mb into only less than 3 kb, making it computationally efficient for further analysis
592 (21). The code for calculating Shape-DNA is written in Python and is freely available
593 (http://reuter.mit.edu/software/shapedna/). We applied the Shape-DNA code to the data and
594 analyzed the resulting eigenvalues using MATLAB.

595 **Eigenvalue normalization**

596 To account for differences in brain sizes among participants, the eigenvalue spectra from Shape-
597 DNA should be normalized (41). Previous studies (21, 38, 46) have applied volume normalization
598 to normalize the eigenvalue spectrum to unit volume via the following equation (21, 38):

599 $$\lambda' = v^{2/D}\lambda \quad (2)$$

600 where v is the Riemannian volume of the manifold, λ is the original eigenvalue spectrum ($\lambda = [\lambda^1,$
601 $\lambda^2, \ldots]$), and λ' is the volume normalized eigenvalue spectrum. Although this approach has been
602 used in the literature, it is still unable to isolate shape properties as it does not control the effect of
603 different surface areas among objects. For example, in Figure 7, each line is the eigenvalue
604 spectrum for the cortical surface of one subject, and these eigenvalue spectra are straight lines
605 (although they are not straight lines if we zoom in these figures) increasing along with the indices:
606 each eigen-spectrum line has its own slope. Specifically, slopes of the native eigenvalue spectra

607 from each subject are different (Figure 7A) and related to the volume of the manifold. Even though
608 volume normalization decreases the differences in the slopes of the eigenvalue spectra, the slopes
609 remain quite different (Figure 7B) and are driven by differences in surface area (41). More
610 specifically,

611 $$\lambda n \sim \frac{4\pi n}{\text{area}(M)} \quad (3)$$

612 where λ is the eigenvalue and n is the eigenvalue index. Hence, an appropriate surface area-based
613 normalization is essential to isolate the effects of shape that are distinct from size, particularly
614 given the evidence that the right hemisphere tends to have a greater cortical surface area than the
615 left hemisphere (10). Without surface area normalization, differences between the hemispheres
616 may be primarily driven by differences in the surface area of the two hemispheres.

617 To perform surface area normalization, we obtained the unit surface area by dividing the
618 vertex coordinates on each axis by the square root of the total surface area (Eqs. 4).

619 $$\mathrm{Vx}' = \frac{\mathrm{Vx}}{\sqrt{area(M)}};\ \mathrm{Vy}' = \frac{\mathrm{Vy}}{\sqrt{area(M)}};\ \mathrm{Vz}' = \frac{\mathrm{Vz}}{\sqrt{area(M)}} \quad (4)$$

620 where Vx, Vy, Vz are the coordinates of all vertices on the X-axis, Y-axis, and Z-axis, respectively;
621 area (M) is the surface area of object M; Vx', Vy', Vz' are the coordinates of transformed vertices
622 on the X-axis, Y-axis, and Z-axis respectively. Surface area normalization is stricter than volume
623 normalization for spectral alignment, and the eigenvalue spectra with surface area normalization
624 have a nearly-identical slope (41) (Figure 7C).

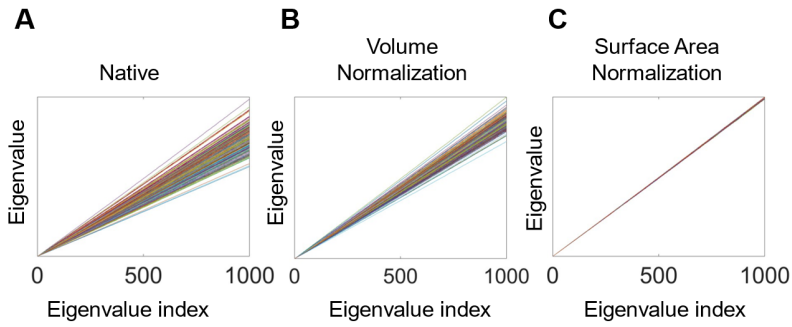

Figure 7. Eigenvalue spectra with and without normalization. (**A**) Native eigenvalue spectra. (**B**) Eigenvalue spectra with volume normalization. (**C**) Eigenvalue spectra with surface area normalization. All of these results are from the left white surfaces of 233 subjects from the OASIS-3 data. Each line represents a subject. The slopes of the spectra in (A) and (B) differ among subjects, whereas those in (C) are almost identical.

The shape asymmetry signature

The LBO eigenvalues measure the intrinsic geometry of an object and are isometry invariant. Hence, the eigenvalue spectra are identical regardless of object positions, rotations, and mirroring (i.e., perfect projection from the brain structure of the right hemisphere to the left does not change the eigenvalue spectrum) (21, 43). Therefore, brain asymmetry can be calculated directly from the eigenvalue spectra of the two hemispheres (21, 38) without image registration or smoothing (21, 43). In this study, after calculating the eigenvalues with surface area normalization, we subtracted the eigenvalue spectra of the right hemisphere from those of the left hemisphere in the same subject

at each spatial scale (each eigenvalue index) to define the shape asymmetry signature (SAS). Formally, the SAS for subject *i* is given by

$$\Lambda^i = \lambda_L^i - \lambda_R^i \quad (5)$$

where λ is the eigenvalue spectrum $\lambda = (\lambda^1, \lambda^2, \ldots, \lambda^n)$ from the left (L) and right (R) hemispheres, each of which represents a certain spatial scale. There are other possible asymmetry indices (10, 78), but those indices are not appropriate for a surface area-normalized eigenvalue analysis, as our normalization already accounts for size effects.

Moodie et al. (78) proposed subtracting the mean of the asymmetry values across subjects (i.e., directional asymmetry) from the individual asymmetry values to represent the fluctuating asymmetry. We tested this approach with our method, and the results were generally the same, as the eigenvalues were normalized before calculating the asymmetry. For simplicity, we defined the SAS using Eqs. 5 in to represent the fluctuating asymmetry.

Subject Identification

Our first aim was to validate the SAS as a useful and robust measure of fluctuating asymmetry. We, therefore, evaluated the extent to which the SAS of each individual subject measured at time 1 (t1) could be used to identify the same person at time 2 (t2) in the longitudinal data, akin to a neuromorphological fingerprint. The t1 – t2 Pearson correlations were then estimated between all pairs of N individuals, resulting in an $N \times N$ correlation matrix. Amico and Goni (52) defined identifiability as the difference between the mean of within-subject correlations (diagonal elements of the Pearson correlation matrix in Figure 1C) and the mean of between-subject correlations (off-diagonal elements of the Pearson correlation matrix in Figure 1C). This approach allows for a more quantitative and finer-grained comparison of the identifiability of different metrics compared to

661 other approaches that just rely on binary identification accuracy (e.g., Finn et al. (47)) (52, 53).
662 However, this approach does not take into account the variance of the observations. To examine
663 the within- and between- subject similarities, we utilized the Glass's Δ, which is the standardized
664 difference between the mean values of two categories of observations, normalized by the standard
665 deviation of a control group (79), which is the between-subject group in our case. Our analysis
666 thus examines how the within-subject correlations differ from between-subject correlations. The
667 Glass's Δ has been recommended when the standard deviations of the two groups are substantially
668 different (79, 80), which is the case for the between- and within- subject groups. Thus, our
669 identifiability score was given by

670 $$Identifiability\ score = \frac{mean(r_{ii}) - mean(r_{ij})}{SD(r_{ij})} \quad (6)$$

671 where *SD* is the standard deviation. Higher scores indicate a greater capacity to discriminate
672 between individuals. We also tested the pooled standard deviation of the two groups (53), as the
673 Cohen's *d*, and the results were generally consistent to those using the Glass's Δ. We also evaluated
674 the identifiability performance of the SAS with respect to unihemispheric descriptors of either
675 combining size and shape or shape alone: namely the eigenvalues (native, volume-normalized, or
676 surface area-normalized) from the same hemispheres between time 1 and time 2 follow-up;
677 concatenating eigenvalues of both left and right hemispheres between time 1 and time 2; and
678 identifying the shape of one hemisphere from the shape of the other hemisphere both at time 1 or
679 both at time 2. We also compared the identifiability score of the SAS to the asymmetry based on
680 commonly used size-related measures (i.e., volume, cortical thickness, and surface area), and
681 resting-state functional connectivity.

682 **Identifying spatial scales for optimum subject identifiability**

Given a surface of N vertices, spectral shape analysis yields up to N eigenvalues, raising the question of how many eigenvalues constitute a sufficient description of cortical shape. Is a full representation of the entire surface necessary for optimal subject identifiability, or can this be achieved using a more compact set of eigenvalues? If so, the specific number of eigenvalues required would define the relevant spatial scale of shape differences that characterize the fluctuating asymmetry at which individual differences are most prevalent.

To address this question, we decompose the cortical surface and use an increasing number of eigenvalues, from the first two eigenvalues (λ^1, λ^2) to the first 1000 eigenvalues (λ^1, λ^2, λ^3, …, λ^{1000}), each time computing the SAS and evaluating subject identifiability. For example, we first quantified the shape of cortical surface using only λ^1 and λ^2, thus capturing the coarsest scales of cortical shape. We then quantified the surface using λ^1 through λ^3, then λ^1 through λ^4, and so on. If there is a specific spatial scale that is optimal for this subject identifiability, we expect to see a peak in the identifiability score as a function of the truncation number, k. This peak not only defines the spatial scale at which individual variability, and thus fluctuating asymmetry, is most strongly expressed, but it also identifies a meaningful point at which to define a compressed summary of fluctuating asymmetry using the eigenvalue spectrum.

Cortical shape harmonics

The cerebral cortex is topologically equivalent to a sphere. Solving the Helmholtz equation for a sphere yields groups of eigenfunctions with the same eigenvalues and spatial wavelength, progressing along orthogonal axes (54). These groups in the solutions to the idealized spherical case are known as the spherical harmonics. The zeroth group (L = 0) is comprised of the first eigenvalue; the first group (L = 1) is comprised of the 2nd, 3rd, and 4th eigenvalues; the second group (L = 2) is comprised of the 5th to 9th eigenvalues, and so on. That is, there are 2 (L + 1) − 1

706 eigenvalues in the Lth group. Robinson et al. (54) showed that while the eigenvalues between the
707 cortical surface and sphere are different, the spherical grouping provides a rough division of the
708 convoluted cortical surface. This is a useful grouping approach to investigate eigenfunctions and
709 eigenvalues as the constituents of each group have roughly the same spatial wavelength. By
710 averaging over several eigenvalues with similar spatial scales, we can also increase the stability of
711 the truncation number across datasets. For example, the peak SAS identifiability appeared at the
712 first 126 and 122 eigenvalues for the OASIS-3 and ADNI data, respectively, and these eigenvalues
713 are all within the 11th eigen-group (L = 11).

714 To estimate the corresponding wavelength of each eigen-group, we used an approximation
715 of the spatial wavelength in the spherical case:

716 $$W = \frac{2\pi Rs}{\sqrt{L(L+1)}} \quad (7)$$

717 where Rs is the equivalent sphere of the original object (for the fsaverage case, Rs is about 67 mm)
718 and L is the index of the eigen-group. We used the population-based template (fsaverage) as an
719 example to show the wavelengths of the first 14 eigen-groups in Appendix 1—Table 1.

720 **Cortical segmentation**

721 We applied the HCP-MMP1 atlas (55) to segment the cortical regions for accessing size-related
722 morphological asymmetry, functional connectivity, and regional volume heritability. This atlas is
723 based on the surface alignment approach, which aligns the images using cortical folding patterns
724 and minimizes the spatial smoothness (55, 81), and thus offers more accurate inter-subject
725 registration than volume-based registration (55). Moreover, regions in the left and right
726 hemispheres of the HCP-MMP1 atlas are corresponding and thus can be used for accessing cortical
727 asymmetry. In addition to the HCP-MMP1 atlas, we also employed the Schaefer atlas (Schaefer

100, 300, and 900) (56) for constructing functional connectivity (FC) and regional volume heritability. The Schaefer atlas has superior functional homogeneity of a parcellation and has different parcellation scales (56); therefore, it can be used for comparing the identifiability of the FC and estimating regional volume heritability at different scales. Specifically, each hemisphere has 50 regions in the Schaefer 100 atlas, 150 regions in the Schaefer 300 atlas, and 450 regions in the Schaefer 900 atlas (56). However, regions in the left and right hemispheres of the Schaefer atlas are not corresponding; therefore, the atlas cannot be used for accessing brain asymmetry.

Non-shape descriptors of brain anatomical asymmetry

To compare identifiability scores obtained with SAS to asymmetries using size-related descriptors, including volume, cortical thickness, and surface area, we had to ensure that the asymmetry values were purely from the asymmetry effect and were not affected by the effect of total brain size. A traditional asymmetry index (13, 19, 35) is:

$$AI^{S,i} = \frac{\left(P_L^{S,i} - P_R^{S,i}\right)}{0.5\left(P_L^{S,i} + P_R^{S,i}\right)} \tag{8}$$

where $AI^{S,i}$ is the asymmetry index for parcellation S of subject i. $P_L^{S,i}$ is the value of the morphological measurement from parcellation S from subject i's left hemisphere; and $P_R^{S,i}$ is from the right hemisphere. However, this asymmetry index is unable to entirely eliminate the effect of total brain size. Here, we use cortical volume as an example. We suppose the total brain volume effect (α) exists, and the effects of each ROI-based volume of the left (Eqs. 9) and right (Eqs. 10) hemispheres are:

$$V_L^{F,i} = \delta_L^i V_L^i + \alpha i \tag{9}$$

$$V_R^{F,i} = \delta_R^i V_R^i + \alpha i \quad (10)$$

where V_L^i and V_R^i are the volumes of region *i* in the left and right hemispheres, respectively, δ_L^i and δ_L^i are the scaling coefficients, and αi is the effect of total brain volume on region i. Thus, $V_L^{F,i}$ and $V_R^{F,i}$ are the overall effects of volume on region *i*. We can apply $V_L^{F,i}$ and $V_R^{F,i}$ to the traditional asymmetry index as in Eqs. 8 to get

$$V_{AI}^i = \frac{[(\delta_L^i V_L^{F,i} + \alpha^i) - (\delta_R^i V_R^{F,i} + \alpha^i)]}{0.5\left[(\delta_L^i V_L^{F,i} + \alpha^i) + (\delta_R^i V_R^{F,i} + \alpha^i)\right]} \quad (11)$$

By re-arranging this equation, we obtain

$$V_{AI}^i = \frac{\delta_L^i V_L^{F,i} - \delta_R^i V_R^{F,i}}{0.5\delta_L^i V_L^{F,i} + 0.5\delta_R^i V_R^{F,i} + \alpha^i} \quad (12)$$

which shows that the total volume effect αi still remains in the denominator and is not removed by the traditional asymmetry index defined in Eqs. 8.

In this study, we adjusted the asymmetry index for the mean of each morphological measurement. Specifically, we revised the traditional asymmetry index by subtracting the mean value of the measurement across all parcellations of each subject before calculating the asymmetry index defined in Eqs. 8. This revised asymmetry measure $RAI^{S,i}$ explicitly calculated as:

$$RAI^{S,i} = \frac{\left(P_L^{S,i} - M^i\right) - \left(P_R^{S,i} - M^i\right)}{0.5\left[\left(P_L^{S,i} - M^i\right) + \left(P_R^{S,i} - M^i\right)\right]} \quad (13)$$

where M^i is the mean value of the measurement across all regions in parcellation of subject *i*. We note that this is an important point, as without this correction, the asymmetry measure is dependent on the mean value.

766 We employed a multi-modal parcellation, HCP-MMP1 version 1.0 (55) on the OASIS-3
767 subjects. We excluded one subject whose cortical surfaces could not be segmented by the HCP-
768 MMP1 atlas. There are 180 regions in each hemisphere of the HCP-MMP1 atlas, including the
769 hippocampus that was excluded in our analysis. We created one vector per asymmetry-index
770 measurement per subject and then used these asymmetry indices in the subject identifiability
771 analyses.

772 **Functional connectivity**

773 We used the resting-state FC from the first session (REST1) in the test sample as the first FC time
774 point (t1) and FC from the first session in the retest session as the second FC time point (t2). We
775 utilized the fMRI signals that were preprocessed by the HCP functional and ICA-FIX pipelines
776 (51). We did not apply any spatial smoothing on the signals. FC was calculated using the upper
777 triangle entries of the Pearson correlation matrix between nodes from the atlas (47). To compare
778 the identifiability of the SAS and the FC across different parcellation scales and atlas, we repeated
779 the FC analysis with the Schaefer 100, 300, and 900 atlas (56) and the HCP-MMP1 atlas (55) from
780 the subjects in the HCP test-retest subsample (n = 44; we excluded one subject without REST1
781 data in one session).

782 **Relationships with sex and handedness.**

783 Sex and handedness are two common characteristics that have been widely examined in the
784 asymmetry literature (3, 4, 7, 10, 11, 13, 14, 20, 21, 25-29, 57). We used a GLM to analyze
785 relationships between each eigenvalue with sex and handedness on 1106 HCP subjects (see *HCP*
786 section).

787 **Relationships with cognition**

We followed Kong et al. (62) and used 13 cognitive measures in the HCP data dictionary that represent a wide range of cognitive functions: namely, (1) Visual Episodic Memory (PicSeq_Unadj); (2) Cognitive Flexibility (CardSort_Unadj); (3) Inhibition (Flanker_Unadj); (4) Fluid Intelligence (PMAT24_A_CR); (5) Reading (ReadEng_Unadj); (6) Vocabulary (PicVocab_Unadj); (7) Processing Speed (ProcSpeed_Unadj); (8) Delay Discounting (DDisc_AUC_40K); (9) Spatial Orientation (VSPLOT_TC); (10) Sustained Attention – Sens (SCPT_SEN); (11) Sustained Attention – Spec (SCPT_SPEC); (12) Verbal Episodic Memory (IWRD_TOT); and (13) Working Memory (ListSort_Unadj). We used PCA to reduce dimensionality and minimize collinearity in the CCA. The first four principal components (PCs) explained 80% of the variance and were retained for our primary analysis. Similarly, we reduced the dimensionality of the SAS measures and ensured equal representation across different spatial scales by taking the mean of the SAS across each eigen-group (from 1st to 11th groups). These 11 mean SAS values and the first four cognitive PCs were then subjected to CCA to identify linear combinations of SAS and cognitive measures that maximally covary with each other (82). Inference on the resulting canonical variates was performed using a permutation-based procedure (61), and robust estimates of canonical loadings were obtained using bootstrapping (83), as described below in the Statistical Analysis section.

Heritability of brain shape

We used monozygotic (MZ) and same-sex dizygotic (DZ) twin pairs and their non-twin siblings to calculate the heritability of brain shape and cortical volume. For twin pairs with more than one non-twin sibling, we selected one sibling at random. We estimated the heritability of each eigenvalue from individual hemispheres and the SAS. To emphasize the importance of properly controlling surface area, we show the heritability of eigenvalues with volume normalization (but

811 without surface area normalization; Figure 6—figure supplement 1). We also calculated the
812 heritability from ROI-based volumes of individual hemispheres (Figure 6—figure supplement 2).
813 Regional cortical volumes of individual hemispheres were estimated for each region of the
814 Schaefer 100, 300, and 900 atlas (56) as well as the HCP-MMP1 atlas (55).

815 Under the assumption that MZ twins are genetically identical whereas DZ twins on average
816 share half of their DNA, structural equation modeling (SEM) can be used to decompose the
817 phenotypic variance of a trait into additive genetic (A), common environmental (C), and unique
818 (subject-specific) environmental (E) factors (75). Twins raised together are likely to share a more
819 common environment compared to their non-twin siblings; therefore, including a set of non-twin
820 siblings into the analysis allows us to additionally separate common environmental contributions
821 into twin-specific (T) and twin non-specific common environmental factors (C). The heritability
822 analyses of brain shape and volume were performed independently using standard SEM
823 implemented in OpenMx software (84, 85) in *R*. For each eigenvalue and parcellated volume,
824 outlying values were first excluded using the boxplot function in *R* keeping data points (v) in a
825 range $Q1-1.5 \times IQR < v < Q3+1.5 \times IQR$, where Q1 and Q3 are the first and third quartiles
826 respectively, and IQR is the interquartile range (75). For each phenotype, we then fitted a set of
827 biometric models – ACTE, ACE, ATE, CTE, TE, CE, E – using age and sex as covariates, where
828 the letters indicate the factors present in the model. The goodness of fit between the models was
829 compared using the Akaike information criterion (AIC) (86), and the best-fitting model for each
830 measure was selected based on the lowest AIC value. Consequently, the heritability for each
831 measure was derived from the best-fitting model, corresponding to the best model that balances
832 the ability to explain data with model complexity. To ensure that the general heritability pattern
833 was not dependent on the model selection, we also calculated the heritability estimates from the

full ACTE model (without model selection) at each eigenvalue (with surface area normalization) of individual hemispheres as well as the SAS. The heritability estimates were highly correlated with those with model selection (Pearson correlation $r = 0.92-0.96$).

Statistical Analysis

We applied a permutation test to evaluate the statistical significance of a given identifiability score for a given number of eigenvalues. We randomly shuffled the subject order of the SAS of the t2 session 50,000 times and then compared the original identifiability score with all the permuted peak identifiability score truncated at each iteration independently to calculate the *P*-value. Statistical inference for models evaluating associations between SAS and sex and handedness was also performed using a permutation test with 100,000 iterations by randomly shuffled the subjects' sex and handedness data. When analyzing associations between the SAS and cognition, we used a recently-developed permutation-based procedure for CCA inference (61) with 50,000 iterations. The *P*-values of the canonical modes were controlled over family-wise error rate (FWER; FWER corrected *P*-values are denoted P_{FWER}), which is more appropriate than the false discovery rate (FDR) when measuring the significant canonical mode (61). The results were consistent when controlling for age and sex as confounding variables. To identify reliable loadings of each SAS eigen-group on the canonical variate, we used bootstrapping with 1000 iterations of the correlation between each SAS eigen-group and the SAS canonical variate. The resulting standard errors were used to estimate z-scores for each loading by dividing the original correlation by the standard errors, and then the z-scores were used to compute two-tailed p-values. We then used FDR (q = 0.05) to correct for multiple comparisons of *P*-values of all the eigen-groups. We also used the same approach to identify reliable correlations of cognitive measures on the corresponding canonical variate. Due to the family structure of the HCP data, we kept the subjects' family

structures intact when shuffling or bootstrapping the subjects using the Permutation Analysis of Linear Models (PALM) software package (*57, 58*).

The statistical significance of the heritability estimates was evaluated through model comparison between models with and without parameter A. For example, if the ACE model was the best-fitting model, the *P*-value was derived by comparing the ACE and CE models; if the best fitting model was CE, we compared this model with the ACE model to get the *P*-value for the A parameter. We also used the same approach for measuring the statistical significance of the common environmental factor (C). FDR ($q = 0.05$) was used to correct for multiple comparisons (corrected *P* values are denoted P_{FDR}) in all analyses except for the CCA, where FWER was controlled using a permutation-based procedure (61).

Data availability

All code and dependent toolboxes used in this study can be found at: https://github.com/cyctbdbw/Shape-Asymmetry-Signature. The code of shape-DNA can be found at: http://reuter.mit.edu/software/shapedna/. The OASIS-3 dataset is available under https://www.oasis-brains.org/. The ADNI dataset is available under https://adni.loni.usc.edu. The HCP dataset is available under https://db.humanconnectome.org/.

Acknowledgments

A.F. was supported by the Sylvia and Charles Viertel Foundation, National Health and Medical Research Council (IDs: 1197431 and 1146292), and Australian Research Council (ID: DP200103509). Data were provided in part by OASIS-3: Principal Investigators: T. Benzinger, D. Marcus, J. Morris; NIH P50 AG00561, P30 NS09857781, P01 AG026276, P01

880 AG003991, R01 AG043434, UL1 TR000448, R01 EB009352. AV-45 doses were provided by
881 Avid Radiopharmaceuticals, a wholly owned subsidiary of Eli Lilly. Data were provided in part
882 by the Human Connectome Project, WU-Minn Consortium (Principal Investigators: David Van
883 Essen and Kamil Ugurbil; 1U54MH091657) funded by the 16 NIH Institutes and Centers that
884 support the NIH Blueprint for Neuroscience Research; and by the McDonnell Center for Systems
885 Neuroscience at Washington University. Data collection and sharing for this project was funded
886 by the Alzheimer's Disease Neuroimaging Initiative (ADNI) (National Institutes of Health Grant
887 U01 AG024904) and DOD ADNI (Department of Defense award number W81XWH-12-2-0012).
888 ADNI is funded by the National Institute on Aging, the National Institute of Biomedical Imaging
889 and Bioengineering, and through generous contributions from the following: AbbVie, Alzheimer's
890 Association; Alzheimer's Drug Discovery Foundation; Araclon Biotech; BioClinica, Inc.; Biogen;
891 Bristol-Myers Squibb Company; CereSpir, Inc.; Cogstate; Eisai Inc.; Elan Pharmaceuticals, Inc.;
892 Eli Lilly and Company; EuroImmun; F. Hoffmann-La Roche Ltd and its affiliated company
893 Genentech, Inc.; Fujirebio; GE Healthcare; IXICO Ltd.; Janssen Alzheimer Immunotherapy
894 Research & Development, LLC.; Johnson & Johnson Pharmaceutical Research & Development
895 LLC.; Lumosity; Lundbeck; Merck & Co., Inc.; Meso Scale Diagnostics, LLC.; NeuroRx
896 Research; Neurotrack Technologies; Novartis Pharmaceuticals Corporation; Pfizer Inc.; Piramal
897 Imaging; Servier; Takeda Pharmaceutical Company; and Transition Therapeutics. The Canadian
898 Institutes of Health Research is providing funds to support ADNI clinical sites in Canada. Private
899 sector contributions are facilitated by the Foundation for the National Institutes of Health
900 (www.fnih.org). The grantee organization is the Northern California Institute for Research and
901 Education, and the study is coordinated by the Alzheimer's Therapeutic Research Institute at the

University of Southern California. ADNI data are disseminated by the Laboratory for Neuro Imaging at the University of Southern California.

Competing interests: Authors declare that they have no competing interests.

References

1. Duboc V, Dufourcq P, Blader P, Roussigne M. Asymmetry of the Brain: Development and Implications. Annu Rev Genet. 2015;49:647-72.
2. Gunturkun O, Strockens F, Ocklenburg S. Brain Lateralization: A Comparative Perspective. Physiol Rev. 2020;100(3):1019-63.
3. Corballis MC, Haberling IS. The Many Sides of Hemispheric Asymmetry: A Selective Review and Outlook. J Int Neuropsychol Soc. 2017;23(9-10):710-8.
4. Gunturkun O, Ocklenburg S. Ontogenesis of Lateralization. Neuron. 2017;94(2):249-63.
5. Esteves M, Ganz E, Sousa N, Leite-Almeida H. Asymmetrical Brain Plasticity: Physiology and Pathology. Neuroscience. 2020.
6. Li X, Crow TJ, Hopkins WD, Gong Q, Roberts N. Human torque is not present in chimpanzee brain. Neuroimage. 2018;165:285-93.
7. Toga AW, Thompson PM. Mapping brain asymmetry. Nat Rev Neurosci. 2003;4(1):37-48.
8. Zhao L, Matloff W, Shi Y, Cabeen RP, Toga AW. Mapping Complex Brain Torque Components and Their Genetic and Phenomic Architecture in 24,112 healthy individuals. Biol Psychiatry. 2021. Available from: https://doi.org/10.1016/j.biopsych.2021.11.002.
9. Kang X, Herron TJ, Ettlinger M, Woods DL. Hemispheric asymmetries in cortical and subcortical anatomy. Laterality. 2015;20(6):658-84.
10. Kong XZ, Mathias SR, Guadalupe T, Group ELW, Glahn DC, Franke B, et al. Mapping cortical brain asymmetry in 17,141 healthy individuals worldwide via the ENIGMA Consortium. Proc Natl Acad Sci U S A. 2018;115(22):E5154-E63.
11. Plessen KJ, Hugdahl K, Bansal R, Hao X, Peterson BS. Sex, age, and cognitive correlates of asymmetries in thickness of the cortical mantle across the life span. J Neurosci. 2014;34(18):6294-302.
12. Gomez-Robles A, Hopkins WD, Sherwood CC. Increased morphological asymmetry, evolvability and plasticity in human brain evolution. Proc Biol Sci. 2013;280(1761): 115-26.
13. Kong XZ, Postema MC, Guadalupe T, de Kovel C, Boedhoe PSW, Hoogman M, et al. Mapping brain asymmetry in health and disease through the ENIGMA consortium. Hum Brain Mapp. 2020.
14. Deep-Soboslay A, Hyde TM, Callicott JP, Lener MS, Verchinski BA, Apud JA, et al. Handedness, heritability, neurocognition and brain asymmetry in schizophrenia. Brain. 2010;133(10):3113-22.
15. Postema MC, van Rooij D, Anagnostou E, Arango C, Auzias G, Behrmann M, et al. Altered structural brain asymmetry in autism spectrum disorder in a study of 54 datasets. Nat Commun. 2019;10(1):4958.
16. Gomez-Robles A, Hopkins WD, Schapiro SJ, Sherwood CC. The heritability of chimpanzee and human brain asymmetry. Proc Biol Sci. 2016;283(1845).

17. Cai Y, Liu J, Zhang L, Liao M, Zhang Y, Wang L, et al. Grey matter volume abnormalities in patients with bipolar I depressive disorder and unipolar depressive disorder: a voxel-based morphometry study. Neurosci Bull. 2015;31(1):4-12.
18. Fling BW, Dutta GG, Schlueter H, Cameron MH, Horak FB. Associations between Proprioceptive Neural Pathway Structural Connectivity and Balance in People with Multiple Sclerosis. Front Hum Neurosci. 2014;8:814.
19. Kurth F, Thompson PM, Luders E. Investigating the differential contributions of sex and brain size to gray matter asymmetry. Cortex. 2018;99:235-42.
20. Nunez C, Theofanopoulou C, Senior C, Cambra MR, Usall J, Stephan-Otto C, et al. A large-scale study on the effects of sex on gray matter asymmetry. Brain Struct Funct. 2018;223(1):183-93.
21. Wachinger C, Golland P, Kremen W, Fischl B, Reuter M, Alzheimer's Disease Neuroimaging I. BrainPrint: a discriminative characterization of brain morphology. Neuroimage. 2015;109:232-48.
22. Kovalev VA, Kruggel F, von Cramon DY. Gender and age effects in structural brain asymmetry as measured by MRI texture analysis. NeuroImage. 2003;19(3):895-905.
23. Guadalupe T, Zwiers MP, Wittfeld K, Teumer A, Vasquez AA, Hoogman M, et al. Asymmetry within and around the human planum temporale is sexually dimorphic and influenced by genes involved in steroid hormone receptor activity. Cortex. 2015;62:41-55.
24. Takao H, Abe O, Yamasue H, Aoki S, Sasaki H, Kasai K, et al. Gray and white matter asymmetries in healthy individuals aged 21-29 years: a voxel-based morphometry and diffusion tensor imaging study. Hum Brain Mapp. 2011;32(10):1762-73.
25. Narr KL, Bilder RM, Luders E, Thompson PM, Woods RP, Robinson D, et al. Asymmetries of cortical shape: Effects of handedness, sex and schizophrenia. Neuroimage. 2007;34(3):939-48.
26. Steinmetz H, Volkmann J, Jancke L, Freund HJ. Anatomical Left-Rght Asymmetry of Languagerelated Temporal Cortex Is Different in Left- and Right-handers. Annals of Neurology. 1991;29:315-9.
27. Good CD, Johnsrude I, Ashburner J, Henson RN, Friston KJ, Frackowiak RS. Cerebral asymmetry and the effects of sex and handedness on brain structure: a voxel-based morphometric analysis of 465 normal adult human brains. Neuroimage. 2001;14(3):685-700.
28. Guadalupe T, Willems RM, Zwiers MP, Arias Vasquez A, Hoogman M, Hagoort P, et al. Differences in cerebral cortical anatomy of left- and right-handers. Front Psychol. 2014;5:261.
29. Maingault S, Tzourio-Mazoyer N, Mazoyer B, Crivello F. Regional correlations between cortical thickness and surface area asymmetries: A surface-based morphometry study of 250 adults. Neuropsychologia. 2016;93(Pt B):350-64.
30. Neubauer S, Gunz P, Scott NA, Hublin JJ, Mitteroecker P. Evolution of brain lateralization: A shared hominid pattern of endocranial asymmetry is much more variable in humans than in great apes. Sci Adv. 2020;6(7):eaax9935.
31. Sherwood CC, Gómez-Robles A. Brain Plasticity and Human Evolution. Annual Review of Anthropology. 2017;46(1):399-419.
32. Francks C. Exploring human brain lateralization with molecular genetics and genomics. Ann N Y Acad Sci. 2015;1359:1-13.
33. de Kovel CGF, Lisgo SN, Fisher SE, Francks C. Subtle left-right asymmetry of gene expression profiles in embryonic and foetal human brains. Sci Rep. 2018;8(1):12606.

34. Graham J, Özener B. Fluctuating Asymmetry of Human Populations: A Review. Symmetry. 2016;8(12).
35. Sha Z, Schijven D, Carrion-Castillo A, Joliot M, Mazoyer B, Fisher SE, et al. The genetic architecture of structural left-right asymmetry of the human brain. Nat Hum Behav. 2021;15:1-4.
36. Nadig A, Seidlitz J, McDermott CL, Liu S, Bethlehem R, Moore TM, et al. Morphological integration of the human brain across adolescence and adulthood. Proc Natl Acad Sci U S A. 2021;118(14). Available from: https://doi.org/10.1073/pnas.2023860118.
37. Gomez-Robles A, Reyes LD, Sherwood CC. Landmarking Brains. 2018:115-26.
38. Wachinger C, Salat DH, Weiner M, Reuter M, Alzheimer's Disease Neuroimaging I. Whole-brain analysis reveals increased neuroanatomical asymmetries in dementia for hippocampus and amygdala. Brain. 2016;139(Pt 12):3253-66.
39. Kruggel F, Solodkin A. Heritability of Structural Patterning in the Human Cerebral Cortex. Neuroimage. 2020;221:117169.
40. Kurth F, Gaser C, Luders E. A 12-step user guide for analyzing voxel-wise gray matter asymmetries in statistical parametric mapping (SPM). Nat Protoc. 2015;10(2):293-304.
41. Reuter M, Wolter FE, Shenton M, Niethammer M. Laplace-Beltrami Eigenvalues and Topological Features of Eigenfunctions for Statistical Shape Analysis. Comput Aided Des. 2009;41(10):739-55.
42. Ge T, Reuter M, Winkler AM, Holmes AJ, Lee PH, Tirrell LS, et al. Multidimensional heritability analysis of neuroanatomical shape. Nat Commun. 2016;7:13291.
43. Reuter M, Wolter F-E, Peinecke N. Laplace–Beltrami spectra as 'Shape-DNA' of surfaces and solids. Computer-Aided Design. 2006;38(4):342-66.
44. Lévy B. Laplace-beltrami eigenfunctions towards an algorithm that "understands" geometry. IEEE International Conference on Shape Modeling and Applications - SMI 2006. 2006:13.
45. Richards R, Greimel E, Kliemann D, Koerte IK, Schulte-Korne G, Reuter M, et al. Increased hippocampal shape asymmetry and volumetric ventricular asymmetry in autism spectrum disorder. Neuroimage Clin. 2020;26:102207.
46. Wachinger C, Nho K, Saykin AJ, Reuter M, Rieckmann A, Alzheimer's Disease Neuroimaging I. A Longitudinal Imaging Genetics Study of Neuroanatomical Asymmetry in Alzheimer's Disease. Biol Psychiatry. 2018;84(7):522-30.
47. Finn ES, Shen X, Scheinost D, Rosenberg MD, Huang J, Chun MM, et al. Functional connectome fingerprinting: identifying individuals using patterns of brain connectivity. Nat Neurosci. 2015;18(11):1664-71.
48. LaMontagne PJ, Benzinger TLS, Morris JC, Keefe S, Hornbeck R, Xiong C, et al. OASIS-3: Longitudinal Neuroimaging, Clinical, and Cognitive Dataset for Normal Aging and Alzheimer Disease. medRxiv [Preprint] 2019. Available from: https://doi.org/10.1101/2019.12.13.19014902 [Accessed 03 Dec 2021].
49. Van Essen DC, Smith SM, Barch DM, Behrens TE, Yacoub E, Ugurbil K, et al. The WU-Minn Human Connectome Project: an overview. Neuroimage. 2013;80:62-79.
50. Fischl B, Salat DH, Busa E, Albert M, Dieterich M, Haselgrove C, et al. Whole Brain Segmentation Automated Labeling of Neuroanatomical Structures in the Human Brain. Neuron. 2002;33(3):341–55.
51. Glasser MF, Sotiropoulos SN, Wilson JA, Coalson TS, Fischl B, Andersson JL, et al. The minimal preprocessing pipelines for the Human Connectome Project. Neuroimage. 2013;80:105-24.

52. Amico E, Goni J. The quest for identifiability in human functional connectomes. Sci Rep. 2018;8(1):8254.
53. Mansour LS, Tian Y, Yeo BTT, Cropley V, Zalesky A. High-resolution connectomic fingerprints: Mapping neural identity and behavior. Neuroimage. 2021;229:117695.
54. Robinson PA, Zhao X, Aquino KM, Griffiths JD, Sarkar S, Mehta-Pandejee G. Eigenmodes of brain activity: Neural field theory predictions and comparison with experiment. Neuroimage. 2016;142:79-98.
55. Glasser MF, Coalson TS, Robinson EC, Hacker CD, Harwell J, Yacoub E, et al. A multi-modal parcellation of human cerebral cortex. Nature. 2016;536(7615):171-8.
56. Schaefer A, Kong R, Gordon EM, Laumann TO, Zuo XN, Holmes AJ, et al. Local-Global Parcellation of the Human Cerebral Cortex from Intrinsic Functional Connectivity MRI. Cereb Cortex. 2018;28(9):3095-114.
57. Kong XZ, Postema M, Schijven D, Castillo AC, Pepe A, Crivello F, et al. Large-Scale Phenomic and Genomic Analysis of Brain Asymmetrical Skew. Cereb Cortex. 2021;31(9):4151-4168.
58. Winkler AM, Webster MA, Brooks JC, Tracey I, Smith SM, Nichols TE. Non-parametric combination and related permutation tests for neuroimaging. Hum Brain Mapp. 2016;37(4):1486-511.
59. Winkler AM, Webster MA, Vidaurre D, Nichols TE, Smith SM. Multi-level block permutation. Neuroimage. 2015;123:253-68.
60. Allen M, Poggiali D, Whitaker K, Marshall TR, Kievit RA. Raincloud plots: a multi-platform tool for robust data visualization. Wellcome Open Res. 2019;4:63.
61. Winkler AM, Renaud O, Smith SM, Nichols TE. Permutation inference for canonical correlation analysis. Neuroimage. 2020;220:117065.
62. Kong R, Li J, Orban C, Sabuncu MR, Liu H, Schaefer A, et al. Spatial Topography of Individual-Specific Cortical Networks Predicts Human Cognition, Personality, and Emotion. Cereb Cortex. 2019;29(6):2533-51.
63. Chen CH, Panizzon MS, Eyler LT, Jernigan TL, Thompson W, Fennema-Notestine C, et al. Genetic influences on cortical regionalization in the human brain. Neuron. 2011;72(4):537-44.
64. Chen CH, Gutierrez ED, Thompson W, Panizzon MS, Jernigan TL, Eyler LT, et al. Hierarchical genetic organization of human cortical surface area. Science. 2012;335(6076):1634-6.
65. Chen CH, Fiecas M, Gutierrez ED, Panizzon MS, Eyler LT, Vuoksimaa E, et al. Genetic topography of brain morphology. Proc Natl Acad Sci U S A. 2013;110(42):17089-94.
66. Eyler LT, Vuoksimaa E, Panizzon MS, Fennema-Notestine C, Neale MC, Chen CH, et al. Conceptual and data-based investigation of genetic influences and brain asymmetry: a twin study of multiple structural phenotypes. J Cogn Neurosci. 2014;26(5):1100-17.
67. Felton A, Vazquez D, Ramos-Nunez AI, Greene MR, McDowell A, Hernandez AE, et al. Bilingualism Influences Structural Indices of Interhemispheric Organization. J Neurolinguistics. 2017;42:1-11.
68. Ronan L, Fletcher PC. From genes to folds: a review of cortical gyrification theory. Brain Struct Funct. 2015;220(5):2475-83.
69. Kruggel F. The macro-structural variability of the human neocortex. Neuroimage. 2018;172:620-30.

70. Valk SL, Xu T, Margulies DS, Masouleh SK, Paquola C, Goulas A, et al. Shaping brain structure Genetic and phylogenetic axes of macroscale organization of cortical thickness. Science Advances. 2020;6(39):eabb3417.
71. Yeo RA, Ryman SG, Pommy J, Thoma RJ, Jung RE. General cognitive ability and fluctuating asymmetry of brain surface area. Intelligence. 2016;56:93-8.
72. O'Bryant SE, Humphreys JD, Smith GE, Ivnik RJ, Graff-Radford NR, Petersen RC, et al. Detecting dementia with the mini-mental state examination in highly educated individuals. Arch Neurol. 2008;65(7):963-7.
73. Jenkinson M, Beckmann CF, Behrens TE, Woolrich MW, Smith SM. Fsl. Neuroimage. 2012;62(2):782-90.
74. Jenkinson M, Bannister P, Brady M, Smith S. Improved Optimization for the Robust and Accurate Linear Registration and Motion Correction of Brain Images. NeuroImage. 2002;17(2):825-41.
75. Arnatkeviciute A, Fulcher BD, Oldham S, Tiego J, Paquola C, Gerring Z, et al. Genetic influences on hub connectivity of the human connectome. Nat Commun. 2021;12(1):4237.
76. Jack CR, Jr., Bernstein MA, Fox NC, Thompson P, Alexander G, Harvey D, et al. The Alzheimer's Disease Neuroimaging Initiative (ADNI): MRI methods. J Magn Reson Imaging. 2008;27(4):685-91.
77. Lian Z, Godil A, Bustos B, Daoudi M, Hermans J, Kawamura S, et al. A comparison of methods for non-rigid 3D shape retrieval. Pattern Recognition. 2013;46(1):449-61.
78. Moodie JE, Ritchie SJ, Cox SR, Harris MA, Munoz Maniega S, Valdes Hernandez MC, et al. Fluctuating asymmetry in brain structure and general intelligence in 73-year-olds. Intelligence. 2020;78:101407.
79. Glass GV, McGaw B, Smith ML. Meta-Analysis in Social Research. 1981.
80. Lakens D. Calculating and reporting effect sizes to facilitate cumulative science: a practical primer for t-tests and ANOVAs. Front Psychol. 2013;4:863.
81. Coalson TS, Van Essen DC, Glasser MF. The impact of traditional neuroimaging methods on the spatial localization of cortical areas. Proc Natl Acad Sci U S A. 2018;115(27):E6356-E65.
82. Smith SM, Nichols TE, Vidaurre D, Winkler AM, Behrens TE, Glasser MF, et al. A positive-negative mode of population covariation links brain connectivity, demographics and behavior. Nat Neurosci. 2015;18(11):1565-7.
83. Dong D, Guell X, Genon S, Wang Y, Chen J, Eickhoff SB, et al. Linking Cerebellar Functional Gradients to Transdiagnostic Behavioral Dimensions of Psychopathology. bioRxiv. 2020.
84. Boker S, Neale M, Maes H, Wilde M, Spiegel M, Brick T, et al. OpenMx: An Open Source Extended Structural Equation Modeling Framework. Psychometrika. 2011;76(2):306-17.
85. Neale MC, Hunter MD, Pritikin JN, Zahery M, Brick TR, Kirkpatrick RM, et al. OpenMx 2.0: Extended Structural Equation and Statistical Modeling. Psychometrika. 2016;81(2):535-49.
86. Akaike H. Information Theory and an Extension of the Maximum Likelihood Principle 949 (Springer, 1998).